Opportunities and Limitations of Partial Transport Quantification in All-Solid-State Composite Electrodes

Sebastian Puls,[1] Lukas Ketter,[2,3] Wolfgang G. Zeier,[1,2,3] Nella M. Vargas-Barbosa*[4]

[1] *Institute of Energy Materials and Devices (IMD), IMD-4: Helmholtz-Institut Münster, Forschungszentrum Jülich, Corrensstrasse 46, Münster 48149, Germany*

[2] *Institute of Inorganic and Analytical Chemistry, University of Münster, 48149 Münster, Germany*

[3] *International Graduate School of Battery Chemistry, Characterization, Analysis, Recycling and Application (BACCARA), University of Münster, 48149 Münster, Germany*

[4] *Chair of Electrochemistry and Bavarian Center for Battery Technology (BayBatt), University of Bayreuth, Universitätsstraße 30, 95448 Bayreuth, Germany*

Abstract:

Microstructure and partial transport are key features that must be optimized in all-solid-state battery (ASSB) composite electrodes. While from the measurement perspective, impedance spectroscopy is a preferred method to determine partial transport because of its speed and simplicity, the interpretation of the impedance spectra can be challenging. This is especially true for ASSB composite electrodes, where two conductive species with similar conductivity are present and transmission line models (TLMs) are often used to fit the spectra. In this study, we present three different TLMs and their impedance responses in Nyquist plots, giving basic insights into how different combinations of circuit elements result in specific spectra, from which partial ionic and electronic conductivities can be calculated. The effects of applied stack pressure and temperature during the measurements on the resulting spectra and their corresponding partial conductivities are evaluated. Combined computational and experimental results show that the partial conductivities and the tortuosity

depend on the thickness of the composite electrode. Moreover, our results demonstrate that well-matched partial transport of ions and electrons in composite electrodes at 0% state-of-charge (SOC) does not directly correlate with superior cycling performance. As such, we report on the limitations of TLMs and advocate for additional techniques to evaluate other microstructural factors such as the contact areas between components that cannot be quantified with transport measurements alone.

Keywords:

All-solid-state battery (ASSB), composite electrode, composite cathode, microstructure, partial transport, transmission line model (TLM)

Introduction:

All-solid-state batteries (ASSBs) are promising next-generation systems with advantageous safety characteristics and offering higher energy densities compared to conventional lithium-ion batteries (LIBs).[1,2] However, the design of ASSB positive electrodes that employ sulfide-based solid electrolytes (SEs) poses challenges different than positive electrodes for LIBs. In LIBs, the liquid electrolyte is added during the battery cell assembly and provides sufficient ionic conduction by filling all pores in the electrodes,[3] while for ASSB positive electrodes, the SE must be incorporated during the preparation of the positive electrode. Therefore, special attention must be paid to the microstructure of the resulting composite electrode, which is influenced by many factors such as the particle size distributions of the materials,[4,5] the compression profiles during processing,[6] the distribution homogeneity of the materials that make up the composite,[7] and the ratio of the materials.[8–10] A key property closely linked to composite electrode microstructure is the partial transport, which must be quantified and optimized in positive electrode composites (CCs, as they are commonly referred to as cathode composites) for good cycling stability and rate capability.

In ASSB positive electrodes, the ionic conductivity is mainly provided by the SE, whereas the positive electroactive material (CAM, as it is commonly referred to as cathode active material), and sometimes carbon-based additives, are responsible for the electronic conductivity. Although there are various

methods to characterize partial transport,[11,12] a potentiostatic electrochemical impedance spectroscopy (PEIS)-based method is favorable because the measurement is done on a timescale of minutes. However, due to the presence of two different mobile conductive species, ions and electrons in the CC in a three-dimensional inhomogeneous volume, the spectra cannot be analyzed with simplified equivalent circuit models but instead need to be fitted with transmission line models (TLMs). The latter have been previously deployed to describe the transport in porous electrodes of LIBs.[13,14] In such cases, the electronic resistance was often neglected due to the much faster electronic transport provided by carbon additives.[15,16] However, due to the reported instabilities of some solid electrolytes against carbon materials,[17,18] the incorporation of conductive additives is not always desirable in ASSBs. In the absence of such additives, the electronic resistance of the composite electrode is non-negligible and complicates the description of the partial transport using TLMs. The latter results in more complex spectra and necessitates the use of TLM models that can be applied to extract partial ionic and electronic conductivities depending on how the measurement was done and the boundary conditions that apply to the system. In particular, the high-frequency response of CCs can be interpreted in various ways including interfaces in the electronic line (describing the interfaces between CAM particles),[5,9] or interfaces in the ionic line (describing the interfaces between SE particles).[19] Moreover, for most porous electrodes used in LIB positive electrodes and also for some ASSB CCs, a contact resistance between the current collector (aluminum, stainless-steel, etc.) and the composite positive electrode is assumed to cause the high-frequency response.[20–23] Geometric impedances and constriction impedances (due to residual porosity) have been reported as the source for additional features (often resembling semicircles) in the impedance spectra.[24,25] While the latter was not intensively investigated for positive composite electrodes yet, they cannot be disregarded. Sometimes, even a combination of multiple factors is presumed and accounted for in the models.[26] Often, no guidance is given why a specific model was chosen for fitting the respective spectra. The different approaches and explanations to describe the impedance spectra of CCs show the challenges

of quantitatively analyzing experimental impedance data without (preliminary) assumptions that may lead to overfitting or fits with minimal physical relevance.

The present study provides basic insight into how different resistances in TLMs show up in Nyquist plots of CCs, the characteristic features of the resulting impedance spectra, how the spectra are influenced by the addition of different circuit elements, and the challenges of assigning such features to specific electrochemical processes. In a practical approach, a CC based on $LiNi_{0.83}Mn_{0.06}Co_{0.11}O_2$ (NMC 83:6:11) and Li_6PS_5Cl is used to validate two different possible TLMs by varying the ratio of the materials. The influence of various measurement parameters such as composite electrode thickness, stack pressure, resting time and heating steps on the measured impedance spectra and the resulting partial transport properties is shown. To support the experimental findings, numerical simulations were carried out on the thickness dependence of partial transport. In the final step, we link partial transport and cycling properties and highlight additional factors that are not covered by the partial transport measurements but that have a significant influence on cycling properties. The basic understanding of various parameters is important, as *e.g.* the results of symmetrical cells may not be applicable to battery (half) cells used for cycling, if different thicknesses were used for both measurement types. This work is an important first step to provide a better understanding of how partial conductivities should be measured, and it shows potential pitfalls that should be avoided to obtain reliable, comparable data that is applicable to battery cells used for cycling.

Experimental

Materials. Li_6PS_5Cl (*MSE Supplies*, 99.99%, Mesh *325*) solid electrolyte (SE) was commercially sourced and exhibited a total ionic conductivity of ≈2.2 $mS \cdot cm^{-1}$ at 25 °C, the corresponding impedance spectrum is depicted in Figure S13. Single crystalline $LiNi_{0.83}Mn_{0.06}Co_{0.11}O_2$ (NMC 83:6:11, *MSE Supplies*) with a D50 of ≈ 3 µm and single crystalline $LiNi_{0.60}Mn_{0.20}Co_{0.20}O_2$ (NMC 622, *MSE supplies*) were used as cathode active materials (CAMs) and dried for 24 h at 150 °C prior to measurements.

The electronic conductivity of pure NMC 83:6:11 was considered 5.22 $mS \cdot cm^{-1}$ for the simulations, as measured elsewhere.[27]

Composite cathode preparation. All composites were prepared in an Ar-filled glovebox (O_2 < 1.5 ppm and H_2O < 0.3 ppm). For the preparation of the cathode composites (CCs) for the conductivity measurements, the SE and the CAM were mixed in a ball mill (*Pulverisette 23, Fritsch GmbH*) for 15 minutes at 15 Hz using 5 mm diameter ZrO_2 balls. Three different weight ratios, 60:40, 70:30 and 80:20, were tested.

Cell assembly. All cell assemblies were carried out under inert atmosphere in an argon-filled glovebox (O_2 < 1.5 ppm and H_2O < 0.3 ppm). We utilized three different cell setups to characterize the CC. Firstly, the partial ionic and electronic conductivities of the CCs were determined. For the measurement of partial ionic conductivity, a symmetrical electron-blocking cell setup SS|In/$(InLi)_x$|SE|CC|SE|In/$(InLi)_x$|SS was used. 60 mg of the SE powder was transferred into the PEEK cell casing and distributed homogeneously and carefully hand-pressed, followed by a carefully distributed 100 mg layer of CC and finally a second 60 mg SE layer. The whole setup was uniaxially pressed at 380 MPa (*Atlas Autotouch Press 25t*, *Specac Ltd.*, for 5 min. An In/$(InLi)_x$ alloy was prepared by pressing together indium foil (*MaTeck GmbH*, 99.999%, 0.1 mm thickness, 9 mm diameter, 45-48 mg) and lithium (*MaTeck GmbH*, 99.8%, 1.5-1.6 mg, 6 mm diameter). The alloy was introduced on both sides of the three-layered pellet to serve as a lithium reservoir, measurements were performed under constant pressure of 50 MPa. The influence of the two SE and In/$(InLi)_x$ was tested in a reference cell, where 120 mg of SE was pressed at 380 MPa for 5 min and afterwards, In/$(InLi)_x$ was attached on both sides. The partial electronic conductivity measurements were performed in an ion-blocking cell setup SS|CC|SS. 100 mg of the CC was uniaxially pressed into a pellet at 380 MPa for 5 minutes, resulting in a ≈50 µm thick layer. Afterwards, a frame pressure of 50 MPa was applied during measurements.

Lastly, the ASSB cells were prepared for the investigation of cycling stability. For the separator layer, 60 mg of pristine Li_6PS_5Cl were pressed into a 10 mm PEEK inlay. 12 mg of the respective CC sample were evenly distributed on the separator layer. The whole setup was uniaxially pressed at 380 MPa for 5 minutes. An In/$(InLi)_x$ alloy anode was prepared as described above and was added to the opposite side of the separator. Measurements were performed at a frame pressure of 50 MPa.

Heat treatment. Some cells monitor the temperature-dependence of the impedance of CCs over a range of 25 °C, 40 °C, 60 °C, 40 °C and 25°C. Each heating step is followed by 2 h of equilibration and a PEIS measurement. The heat was controlled in a *Binder Kühlinkubator KT115.* Different CCs were prepared with NMC 83:6:11 or NMC 622 as CAMs and Li_6PS_5Cl as SE.

PEIS measurements. All PEIS measurements were performed with a *Biologic VSP-300* potentiostat. The amplitude was set to 10 mV, the frequency range was adjusted for the different setups. For the partial ionic conductivity measurement, the frequency range was 7 MHz to 50 mHz, and for the partial electronic conductivity measurement, it was 7 MHz to 25 mHz. The error bars originate from measurements of at least three different cells per sample. To check the consistency of the measurements, three measurements were performed for each cell. The PEIS measurements were performed 2 h, 4 h and 10 h after assembly to check the consistency of the measurement. If PEIS spectra are shown, a representative measurement after 4 h is depicted.

PEIS spectra fitting procedure. The fitting of the impedance spectra was done using the RelaxIS 3 software (*rhd Instruments*) using the SDK option where we implemented the code for T-type TLM model. The spectra were tested for linearity via Kramer-Kronig relations and the high-frequency cutoff adjusted accordingly prior to fitting.

Measurement under controlled pressure. The measurements at controlled pressures were conducted with a *Compre Drive* (*rhd instruments*). A cell was prepared with 144 mg CC filled into the cell (12 mm diameter, 59 µm thickness), performing the measurements at the same loading as the other measurements. The cell was then pressed at 380 MPa for 5 min. Then, a pressure of 50 MPa was

applied. After 2 h of equilibration, PEIS was measured (10 mV amplitude, frequency range between 1 MHz and 100 mHz). The pressure was reduced in steps of 10 MPa down to 10 MPa, each pressure step followed by 5 min of equilibration and a PEIS measurement. Then, the pressure was set back to 50 MPa and held constant, while the temperature was increased to 60 °C and decreased back to 25 °C. Each temperature variation was followed by 2 h of equilibration and a consecutive PEIS measurement.

Cycling. All cells were cycled under constant pressure of 50 MPa at 25 °C with symmetric constant current (*j* at a rate of 1C corresponds to values between 1.83 mA cm^{-2} and 2.44 mA cm^{-2}) charging and discharging at a *MACCOR Battery Tester*. The voltage window was set between 3.0 V and 4.3 V *vs.* Li^+/Li (assuming that 0 V *vs.* In/InLi = 0.62 V *vs.* Li^+/Li).[28] After 5 h of equilibration, the cells underwent a pre-treatment process of five cycles, starting with two cycles at 0.05C (calculated with a theoretical capacity of 200 mAh g^{-1} for the CAM), followed by one cycle at 0.1C, a fourth at 0.05C and a fifth at 0.1 C. After that, for the cells with the different CAM:SE ratios, the C-rate was increased from 0.2C to the final C-rate of 0.5C and then cycled for 300 cycles at the 0.5C rate. Each CC composition was cycled at least in cell triplicates.

Simulations. To study transport as a function of volume fraction, particle size and electrode length, virtual microstructures were generated (Figure S4). In the first step, composites consisting of 300 x 300 x 300 voxels were built with each cubic voxel representing a volume of $(5/3\ \mu m)^3$. The number of voxels describing either SE or CAM domains is determined by the specified volume fractions. By clustering voxels representing solid electrolyte domains as described previously,[27] particle size effects can be studied. While no clustering has been applied to build virtual composites containing SE particles with $d \approx 2$ µm (Figure S4a), cluster sizes of 110 voxels, 1000 voxels and 10000 voxels were specified to generate composites $d \approx 10$ µm, 21 µm and 45 µm (Figure S4d). In a second step, each microstructure was divided into 2, 5, 10 and 20 equally sized parts along the x-axis. Each of the slices corresponds to an electrode of length 250 µm, 100 µm, 50 µm and 25 µm, respectively. The microstructures have been visualized using the software *paraview*.[29]

Effective conductivities were calculated using a resistor network model.[27] The effective ionic conductivity of the composites, the ionic conductivity of the SE phase was specified as 2.2 mS·cm^{-1}, whereas the CAM phase was taken as ionically insulating. Conversely, to calculate effective electronic conductivities, the conductivity of the CAM phase was set to 5.22 mS·cm^{-1},[27] while the SE phase was taken as electronically insulating.

The *pytrax* package was used to compute tortuosities of the virtual microstructures.[30] In each simulation, 10^4 walkers were initially placed randomly in the solid electrolyte and CAM domains to investigate tortuosities of the ion- and electron conducting pathways respectively. Every time step the walkers are then allowed to move to a neighboring site along the three spatial directions in the virtual microstructure. To avoid spatial confinement of the random walkers, they enter mirrored microstructure images when crossing the boundaries. A total of 10^6 time steps per walk was chosen to exclude artifacts from closed pores. From the average axial square displacements (ASD_i) of all walkers as a function of the number of timesteps (t), the axial tortuosities (τ_i) are calculated via

$$\tau_i = \frac{t}{N \cdot \mathrm{ASD}_i}, \qquad \text{(Eq. 7)}$$

with N representing the dimensionality.[30]

Results and Discussion

The efficient transport of ions and electrons in a composite positive electrode is necessary to enable good cycling performance in ASSBs. Unlike mixed ionic electronic conductors in solid oxide fuel cells, where ionic and electronic transport is provided by one material,[31–33] the transport of ions and electrons in composite positive electrodes is enabled by different materials, the SE and CAM, respectively. As such, a consistent interparticle connectivity throughout the composite electrode volume enables the efficient transport of both charged species. To quantify the partial transport in CCs, two different cell setups are used for the PEIS measurements. The ion-blocking setup consists of

the CC being sandwiched between two stainless-steel contacts (Figure 1a). The stainless-steel contacts are blocking for ions and conducting for electrons, allowing the determination of the partial electronic conductivity of the CC at low frequencies. The electron-blocking cell setup is used for the measurement of the partial ionic conductivity at low frequencies (Figure 1b). The two solid electrolyte (SE) layers sandwiching the CC block the transport of electrons across the whole cell and the In/$(InLi)_x$ alloy electrodes attached on both ends serve as lithium reservoirs.

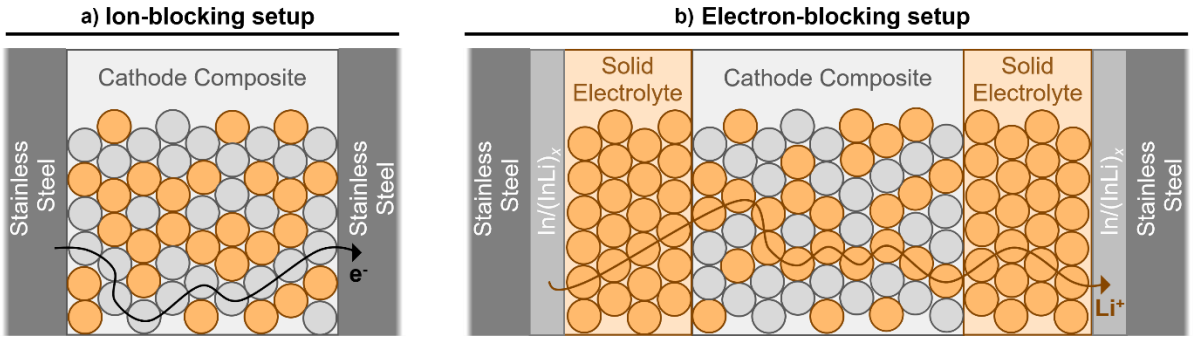

Figure 1: Schematic illustration of the cell setups used to quantify partial transport in composite electrodes, the arrows indicate the transport of the unblocked species, which can be quantified at low frequencies via TLM fitting of the impedance spectra. a) Shows the ion-blocking setup used to determine the electronic conductivity, b) the electron-blocking setup used to determine the ionic conductivity in the composite.

Typically, TLMs are used for analyzing the resulting impedance spectra from the setups shown in Figure 1. Such TLMs typically consist of two lines running in parallel that describe how the ions and electrons are moving. Each line includes an infinite series of circuit elements. Between those two lines, there is at least a capacitor present to describe the interaction between both charged species in the CC. Here, we use a T-type TLM as initially derived by Siroma *et al.*[34,35] It describes symmetrical cell setups with terminals for the same conducting species (electron-electron or ion-ion connection) on both sides. This results in a Li^+-Li^+ connection in the electron-blocking case and an electron-electron connection in the ion-blocking one. Equation 1 describes the T-type TLM frequency-dependent partial transport in the CC under ion-blocking conditions:[34]

$$Z_{\mathrm{CC}}(\omega) = \frac{z_{\mathrm{ion}}\, z_{\mathrm{el}}}{z_{\mathrm{ion}} + z_{\mathrm{el}}} L + \frac{2\, {z_{\mathrm{el}}}^2 \sqrt{z_{\mathrm{int}}}}{(z_{\mathrm{ion}} + z_{\mathrm{el}})^{\frac{3}{2}}} \cdot \frac{\cosh\left(L \sqrt{\frac{z_{\mathrm{ion}} + z_{\mathrm{el}}}{z_{\mathrm{int}}}}\right) - 1}{\sinh\left(L \sqrt{\frac{z_{\mathrm{ion}} + z_{\mathrm{el}}}{z_{\mathrm{int}}}}\right)} \qquad \text{(Eq. 1)}$$

with z_{ion} ($\Omega \cdot \mathrm{cm}^{-1}$) describing the impedance of the ions, z_{el} ($\Omega \cdot \mathrm{cm}^{-1}$) describing the impedance of the electrons, and z_{int} ($\Omega \cdot \mathrm{cm}$) the interfacial impedance between the electronic and ionic path. The length of the TLM, which corresponds to the thickness of the CC, is denoted by L (cm). For the description of the electron-blocking setup, z_{ion} and z_{el} must be interchanged in Eq. 1, which only affects the term $\frac{2\, {z_{\mathrm{el}}}^2 \sqrt{z_{\mathrm{int}}}}{(z_{\mathrm{ion}} + z_{\mathrm{el}})^{\frac{3}{2}}}$ (for the full equation, see Eq. S1).

Prior to fitting the experimental data, the elements z_{ion}, z_{el} and z_{int} must be defined. The simplification of neglecting electronic resistance ($z_{\mathrm{el}} = r_{\mathrm{el}} = 0$), which is often done for LIBs due to the presence of highly conductive carbon additives, is not valid for ASSB positive electrodes, if the partial electronic and ionic conductivities are in the same range. Thus, the requirement to consider z_{el} makes the fitting and understanding of the resulting impedance spectra more challenging. To provide a better understanding of how different impedances show up in PEIS spectra and affect the response, three different T-type TLM models are considered here, and the corresponding simulated spectra are shown in the following.

Comparison of different Transmission Line Models

In the *basic* model, ionic and electronic impedances are described each by a resistor only, and the interfacial impedance between the two lines is described by a constant phase element (CPE). This model describes a system in which the ions move at a certain rate in a single phase (in our case, the SE, described by r_{ion}), and the electrons move at a certain rate in another single phase (in our case the CAM, described by r_{el}). The CPE q_{int} describes the contact between these two phases in which some charge accumulation and/or potential difference is expected. Here, we model a CPE instead of a pure capacitor to capture non-ideal capacitive behavior due to the heterogenous nature of the interface between the two phases in a CC. For our analysis, charge transfer between the SE and CAM is not

considered, as the charge transfer resistance is very high for pristine, uncharged NMC (0% state-of-charge, SOC). With this model, we can recast the impedance of the CC in the ion-blocking setups as

$$Z_{CC}(\omega) = \frac{r_{ion}\, r_{el}}{r_{ion} + r_{el}} L + \frac{2\, {r_{el}}^2 \sqrt{q_{int}^{-1}(i\omega)^{-\alpha}}}{(r_{ion} + r_{el})^{\frac{3}{2}}} \cdot \frac{\cosh\left(L\sqrt{\frac{r_{ion} + r_{el}}{q_{int}^{-1}(i\omega)^{-\alpha}}}\right) - 1}{\sinh\left(L\sqrt{\frac{r_{ion} + r_{el}}{q_{int}^{-1}(i\omega)^{-\alpha}}}\right)} \qquad \text{(Eq. 2)}$$

Note that the resistances r_{ion} and r_{el}, written as lowercase letters, are incremental resistances whereas the overall resistances R_{ion} and R_{el} are written as capital letters and describe the whole resistance throughout the composite. Here, the overall resistances can be calculated from the incremental ones (r_{ion}, r_{el}) by multiplying by the length L. The ion- and electron-blocking *basic* TLMs and the corresponding simulated spectra are depicted in Figure 2a-c.

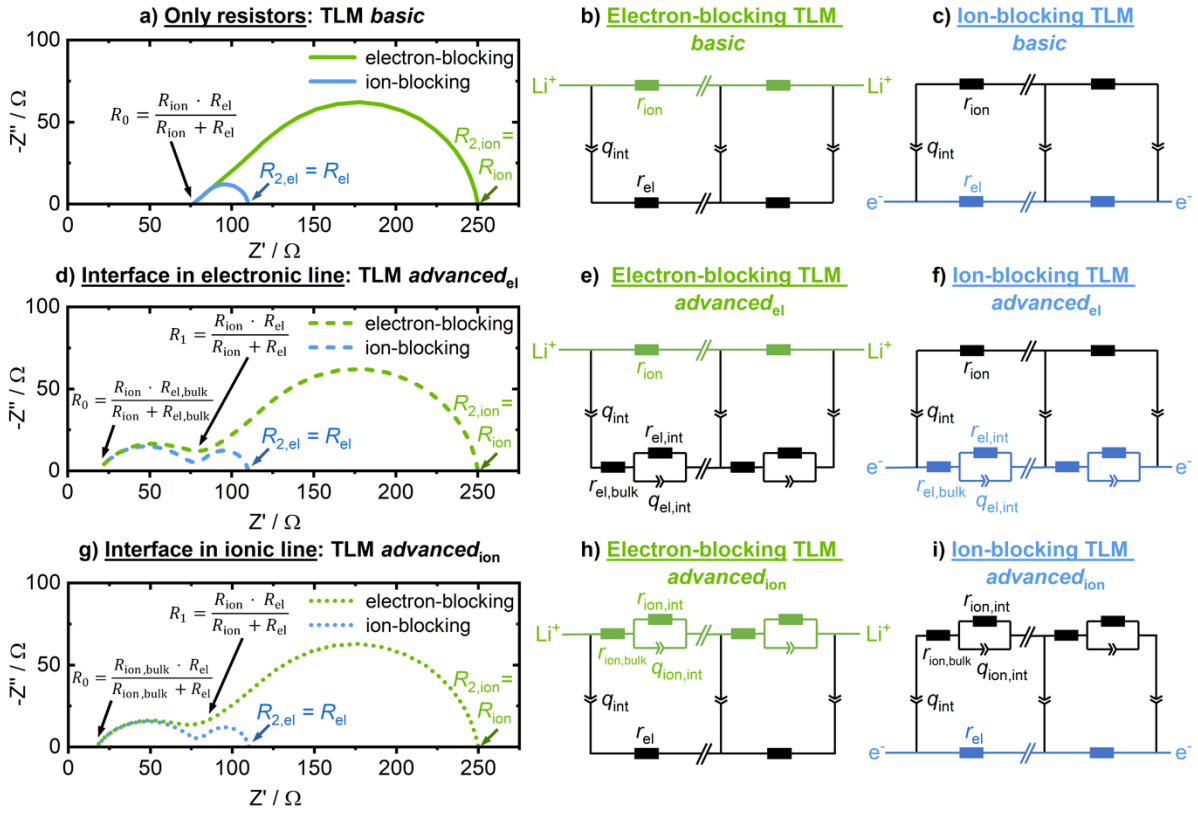

Figure 2: Overview of different T-type transmission line models (TLM) and the corresponding modelled spectra. a) Nyquist spectra for the *basic* electron- and ion-blocking TLMs shown in b) and c), where only resistive elements (r_{ion}, r_{el}) were considered to describe the transport in the electronic and ionic lines. Here, R_{ion}, R_{el} were set to 250 Ω, 110 Ω, respectively.

d) Nyquist spectra for the *advanced*$_{el}$ TLM models shown in e) and f), where R ($r_{el,int}$) and *CPE* ($q_{el,int}$) elements connected in parallel are in series to a bulk resistor ($r_{el,bulk}$) in the electronic line. Here, R_{ion} was fixed at 250 Ω and R_{el} was split up into 20 Ω for $R_{el,bulk}$ and 90 Ω for $R_{el,int}$, for a total R_{el} of 110 Ω. g) Nyquist spectra for the *advanced*$_{ion}$ TLM models shown in h) and i), where R ($r_{ion,int}$) and *CPE* ($q_{ion,int}$) elements connected in parallel are in series to a bulk resistor ($r_{ion,bulk}$) in the ionic line are considered instead. Here, R_{el} was fixed at 110 Ω, but R_{ion} was split up into 20 Ω for $R_{ion,bulk}$ and 230 Ω for $R_{ion,int}$, for a total R_{ion} of 250 Ω. Note that the overall resistances (R) are calculated from the incremental ones (r) by multiplication with L. For all models, the length of the TLM (L) was fixed at 1 cm to better demonstrate the appearance of the values. A CPE (q_{int} = $1 \cdot 10^{-3}$ F·s$^{\alpha-1}$·cm^{-1}) describes the contact between the lines.

The Nyquist plot for the *basic* TLMs (Figure 2a) shows one arc in both the ion-blocking and in the electron-blocking setup, respectively. These arcs possess a characteristic shape, sometimes referred to as "half-teardrop shape", which is mostly known for mixed ionic and electronic conductors that show electronic and ionic conductivities of similar magnitude.[31,32] The spectra show two intercepts at the real impedance axis, a high-frequency intercept R_0, followed by a 45° angle response, and a low-frequency intercept R_2. Both the ion- and the electron-blocking spectra share the same intercept R_0 because at these timescales, both electrons and ions move within the applied electric field in the bulk. Thus, R_0 corresponds to the transport of both species and can be described as follows:[33]

$$R_0{}^{-1} = R_{\mathrm{ion}}{}^{-1} + R_{\mathrm{el}}{}^{-1} \Leftrightarrow R_0 = \frac{R_{\mathrm{ion}}\, R_{\mathrm{el}}}{R_{\mathrm{ion}} + R_{\mathrm{el}}} \qquad \text{(Eq. 3)}$$

At very low frequencies, the blocking electrodes (or electrolyte layers) are entirely impermeable for the blocked species, and only the non-blocked species moves entirely across the CC. Thus, the intercept at low frequencies (R_2) approaches the total resistance of the unblocked charge carrier, which leads to $R_{2,ion} = R_{ion}$ (set to 250 Ω) for the electron-blocking case and $R_{2,el} = R_{el}$ (set to 110 Ω) for the ion-blocking case (Figure 2a). It must be noted that these approximations only apply for a system with ideally blocking electrodes, *i.e.* those that provide full reversibility for the unblocked species and perfectly blocking conditions for the blocked species.

In the second model, *advanced*$_{el}$, an additional parallel *R*/*CPE* element is added in the electronic line. Thus, one resistor in the electronic line represents the bulk electronic resistance of the CAM particles, whereas the additional parallel *R*/*CPE* describes the CAM particle-particle interface.[5,7,9] The models and resulting spectra are shown in Figures 2d-f. Here, $R_{el,bulk}$ was set to 20 Ω and $R_{el,int}$ to 90 Ω, giving a total $R_{el} = R_{el,bulk} + R_{el,int}$ = 110 Ω, which is the total electronic resistance used in the *basic* model. The spectra simulated with the *advanced*$_{el}$ model show two semicircles, a suppressed high-frequency and a drop-shaped low-frequency semicircle. The transition from one semicircle to the next is characterized by a mid-frequency resistance (R_1) defined by

$$R_1 = \frac{R_{\text{ion}}\, R_{\text{el}}}{R_{\text{ion}} + R_{\text{el}}} \qquad \text{(Eq. 4)}$$

This mid-frequency intercept R_1 is equal to the high frequency intercept R_0 in the *basic* model and is the same in both the ion- and electron-blocking case. The additional semicircle approaches a different high frequency value $R_{0,advanced_{\text{el}}}$ compared to the *basic* spectra in Figure 2a, as it is shifted to lower resistances in the case of the *advanced*$_{el}$ model. $R_{0,advanced_{\text{el}}}$ is determined by $R_{el,bulk}$ instead of the total resistance R_{el}, and it applies for both the ion- and electron-blocking spectra:

$$R_{0,advanced_{\text{el}}} = \frac{R_{\text{ion}}\, R_{\text{el,bulk}}}{R_{\text{ion}} + R_{\text{el,bulk}}} \qquad \text{(Eq. 5)}$$

Irrespective of the setup, however, the values of R_2 are exactly the same as in the basic model ($R_{2,ion}$ = 250 Ω, and $R_{2,el}$ = 110 Ω), emphasizing the robustness of the values obtained at low frequencies to describe the net partial transport of the unblocked species in composite electrodes when using the right cell setup. Finally, we consider the *advanced*$_{ion}$-model, where the additional parallel *R*/*CPE* element is incorporated in the ionic line instead, to describe *e.g*. the contribution of grain boundaries between SE particles (Figures 2g-i).[19] Here, $R_{ion,bulk}$ is set to 20 Ω and $R_{ion,int}$ to 230 Ω to match the total R_{ion} as used previously (250 Ω). The spectra look like those of the *advanced*$_{el}$ model with the appearance of two semicircles, the only difference is the high frequency resistance, which is now defined as:

$$R_{0,advanced_{\mathrm{ion}}} = \frac{R_{\mathrm{el}}\, R_{\mathrm{ion,bulk}}}{R_{\mathrm{el}} + R_{\mathrm{ion,bulk}}} \qquad \text{(Eq. 6)}$$

It is evident that in both *advanced* models, *i.e.* irrespective of whether an interfacial contribution is part of the ionic or electronic line, similar high-frequency semicircles are observed in both the ion- and electron-blocking spectra. This makes the assignment of high frequency arcs to a particular process difficult, as there are two conducting species with many possible ionic or electronic conducting interfaces, decomposition products and interphases. However, the total resistance (R_2) is not affected by interfacial processes within the TLM. This is evident by the invariability of R_2 across all models, *basic* and *advanced*.

Finally, for the analysis of the electron-blocking spectra, it is necessary to consider the two SE and $(In/InLi)_x$ layers that sandwich the CC. To determine their influence on the spectra, a reference PEIS measurement was performed on a cell with SE sandwiched between two $In/(InLi)_x$ (*i.e.* $In/(InLi)_x|SE|In/(InLi)_x$) only. The spectrum of this reference cell (Figure S1a) shows a depressed semicircle and was fitted with a resistor R_{SE} describing the resistance of the SE layer, and a parallel $R_{SE|In/(InLi)x}$-*CPE* element describing the two $In/(InLi)_x|SE$ interfaces. These elements must be connected in series before the TLM to describe the two additional layers in the electron-blocking setup (Figure S1b). This addition to the TLM results in a shift of the spectrum by the value of R_{SE} (towards higher resistances) and the $In/(InLi)_x|SE$ interface appears as part of the low-frequency semicircle. Thus, the low-frequency intercept $R_{2,ion}$ of the electron-blocking spectrum, which was equivalent to R_{ion} in all three modeled spectra above, is now shifted by the values of R_{SE} and $R_{SE|In/(InLi)x}$ and is therefore equivalent to $R_{ion}+R_{SE}+R_{SE|In/(InLi)x}$. The shift of the spectra by these additional resistances is depicted in Figure S2. A contact resistance, which may appear in ion-blocking measurements between the stainless-steel electrode and the CC, would shift the spectrum in a similar way.

Validation of the Transmission Line Models via varying CAM:SE

To validate the TLM, PEIS spectra were measured for three different CAM:SE ratios: 61:39 vol%, 48:52 vol% and 37:63 vol%. The ion- and electron-blocking spectra and the resulting conductivities are shown in Figure 3.

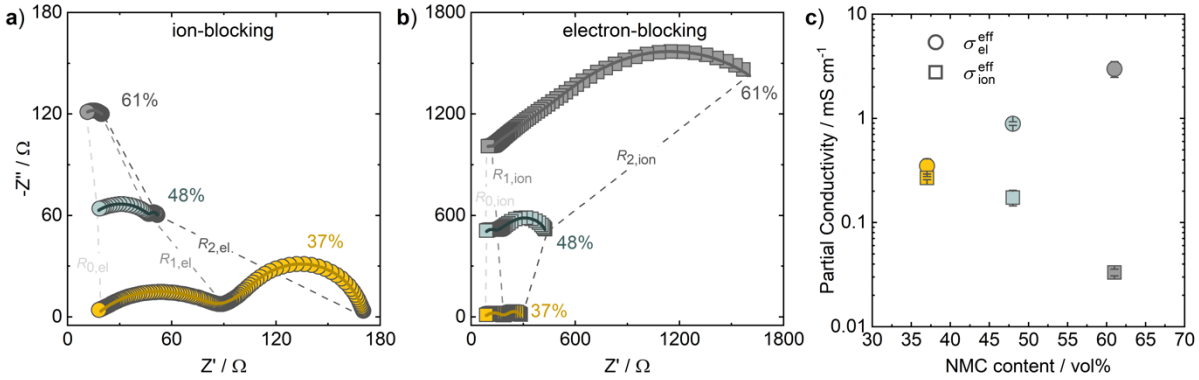

Figure 3: Representative impedance spectra for different positive electroactive material (CAM)-to-solid electrolyte (SE)-ratios, measured in symmetric a) ion-blocking and b) electron-blocking measurement setups. The symbols indicate the measured data, the lines the TLM fit using the *advanced*$_{el}$ model. R_0 indicates the high-, R_1 the mid- and R_2 the low-frequency intercepts, the dashed lines highlight the evolution of the intercepts at different ratios. The percentage indicates the vol% of CAM in the composite electrode. c) Partial conductivities obtained from the fittings of the spectra via TLMs, the electronic conductivities are obtained from the ion-blocking, the ionic conductivities from the electron-blocking measurement. For all samples, the thickness of the CC was in the order of 500 µm.

Since the CAM is the only electron conductor in the CC, we expect a decrease in the partial electronic conductivity ($\sigma_{eff,el}$) as the content of the CAM is reduced. Figure 3a shows precisely this trend: as the vol% of CAM decreases, the low-frequency intercept $R_{2,el}$ increases. Conversely, in the electron-blocking configuration (Figure 3b), we observe a decrease in the low-frequency intercept $R_{2,ion}$ which is consistent with the CC increasing its partial ionic conductivity ($\sigma_{eff,ion}$). Figure 3c summarizes these results more clearly: $\sigma_{eff,ion}$ increases and $\sigma_{eff,el}$ decreases as the vol% of CAM decreases in the CC. Regarding the high- and mid-frequency intercepts, less CAM leads to a similar increase of both $R_{1,ion}$ and $R_{1,el}$, which is due to their definition by $\frac{R_{ion}R_{el}}{R_{ion}+R_{el}}$, and they should be the same after subtracting R_{SE} and $R_{SE|In/(InLi)x}$ from $R_{1,ion}$. The high-frequency intercepts $R_{0,ion}$ and $R_{0,el}$ are higher for lower CAM contents.

To identify the appropriate TLM to be used from those outlined above, fitting was performed with both the *advanced*$_{ion}$ and *advanced*$_{el}$ models (see Table ST1 for detailed resulting fits). Note that the *basic* model was not considered as two processes and not a single half-teardrop shaped spectra was observed irrespective of the setup or CC composition. In order to assess which of the *advanced* models is more appropriate, the anticipated changes in the various resistances were carefully considered for each model as a function of the CC composition. Generally, grain boundary resistances cannot be deconvoluted for pure Li_6PS_5Cl at room-temperature,[36] making *advanced*$_{ion}$ the less suitable model. Additionally, for the *advanced*$_{ion}$ model to apply, we expect that $R_{ion,int}$ and $R_{ion,bulk}$ should both decrease with less CAM in the CC. However, such a decrease is not observed for $R_{ion,bulk}$. Conversely, if *advanced*$_{el}$ is the correct model, an increase of $R_{el,int}$ and $R_{el,bulk}$ is expected with less CAM, because there are less CAM particles throughout the CC offering bulk and interfacial conductivity, thus increasing their total resistance contribution throughout the CC. This is the case for the values obtained from both the electron- and ion-blocking measurement when fitted with *advanced*$_{el}$. Accordingly, while both models could be used to fit the impedance spectra with low errors in the fitted values, only the fits with the *advanced*$_{el}$ model follow the expected trend and reasonably describes the physics of the composition-dependent CCs. Taken together, the *advanced*$_{el}$ model including electronic bulk and interface resistances ($R_{el,bulk}$ and $R_{el,int}$) is used for all further fittings (with serial connection of R_{SE} and the parallel $R_{SE|In/(InLi)x}$/*CPE* element for the electron-blocking case), neglecting possible influences of a contact resistance and other effects. The comparison of different TLM models should generally be done when a new system is investigated, followed by the comparison and validation of the respective fitting results. The conductivities in Figure 3c were obtained with *advanced*$_{el}$.

Since a very similar TLM is used to fit the spectra of both ion- and electron-blocking cell setups, and since the partial transport of nominally equal CC samples is evaluated, the extraction of the same values for the ionic and electronic resitances would be expected from both measurement setups. To validate the robustness of the TLM *advanced*$_{el}$ model, the fitting results of ion- and electron-blocking

measurement are compared in Table 1, and additionally plotted in Figure S3. In general, the values obtained from the two measurement setups follow the same trend and are in a similar range, but not equal.

Table 1: Comparison between the calculated partial conductivities obtained from the ion-blocking and electron-blocking measurements. $\sigma_{eff,el}$ is usually obtained from R_2 in the ion-blocking measurement, and $\sigma_{eff,ion}$ from R_2 in the electron-blocking measurement. The latter results are depicted in bold. Italicized are the values obtained from "the wrong cell setup". The errors stem from triplicate measurements.

CAM:SE ratio / vol%	$\sigma_{eff,el}$ / mS·cm^{-1}			$\sigma_{eff,ion}$ / mS·cm^{-1}		
	Ion-blocking setup	*Electron-blocking setup*	**Error %** (compared to ion-blocking setup)	**Electron-blocking setup**	*Ion-blocking setup*	**Error %** (compared to electron-blocking setup)
37:63	**0.35 ± 0.06**	*0.21 ± 0.02*	-40%	**0.267 ± 0.009**	*0.36 ± 0.02*	+34%
48:52	**0.89 ± 0.03**	*0.63 ± 0.03*	-29%	**0.17 ± 0.03**	*0.13 ± 0.01*	-24%
61:39	**3.0 ± 0.5**	*1.6 ± 0.2*	-46%	**0.033 ± 0.003**	*0.035 ± 0.009*	+6%

On the one hand, for all three CAM:SE ratios, the electronic conductivity $\sigma_{eff,el}$ is higher when obtained from the ion-blocking setup. Thus, there seems to be a general overestimation of $\sigma_{eff,el}$ in the ion-blocking measurement or a general underestimation in the electron-blocking measurement, respectively. The overestimation cannot be explained by additional resistances (*e.g.* a contact resistance) outside the TLM, as these would further reduce the total electronic resistance and result in even higher values for $\sigma_{eff,el}$. Therefore, it is more likely that the reason for the deviation lies in the electron-blocking measurements, as the cell setup is more complicated and there may be some error due to the consideration of the resistances of the two SE layers and especially the resistances of the SE|In/$(InLi)_x$ interfaces on each side of the composite that might deviate from those of the reference cell. Additionally, in the electron-blocking setup, the CC layer which is sandwiched between the two SE layers is assumed to be perfectly cylindrical and to have planar interfaces. However, in the experimental cell, the interfaces between the CC and LPSCl will be non-planar due to the powder

layers being stacekn on top of each other. This might lead to higher resistances compared to those in the ion-blocking measurements. On the other hand, the values of $\sigma_{eff,ion}$ deviate less, and for two of the three CAM:SE ratios, they are within each other's error ranges. In general, both measurements are suitable for extracting a general trend for R_{ion} and R_{el}, but both measurements should be performed for more reliable values. Namely, to determine $\sigma_{eff,el}$ an ion-blocking setup and for $\sigma_{eff,ion}$ an electron-blocking setup should be employed as the determination of the total resistances at low-frequencies is most reliable.

Thickness-dependent evolution of the ion-blocking spectra

The effective conductivities in composite positive electrodes are usually determined at large thicknesses (≈ 500 µm). However, lab-scale composite positive electrodes used for cycling are usually much thinner (between 30 µm and 120 µm). To evaluate if conductivities and tortuosities show a thickness-dependence and to test the ability of TLMs to describe the spectra of thinner composite positive electrodes, we measured the impedance of the 48:52 CAM:SE CC at three different thicknesses.

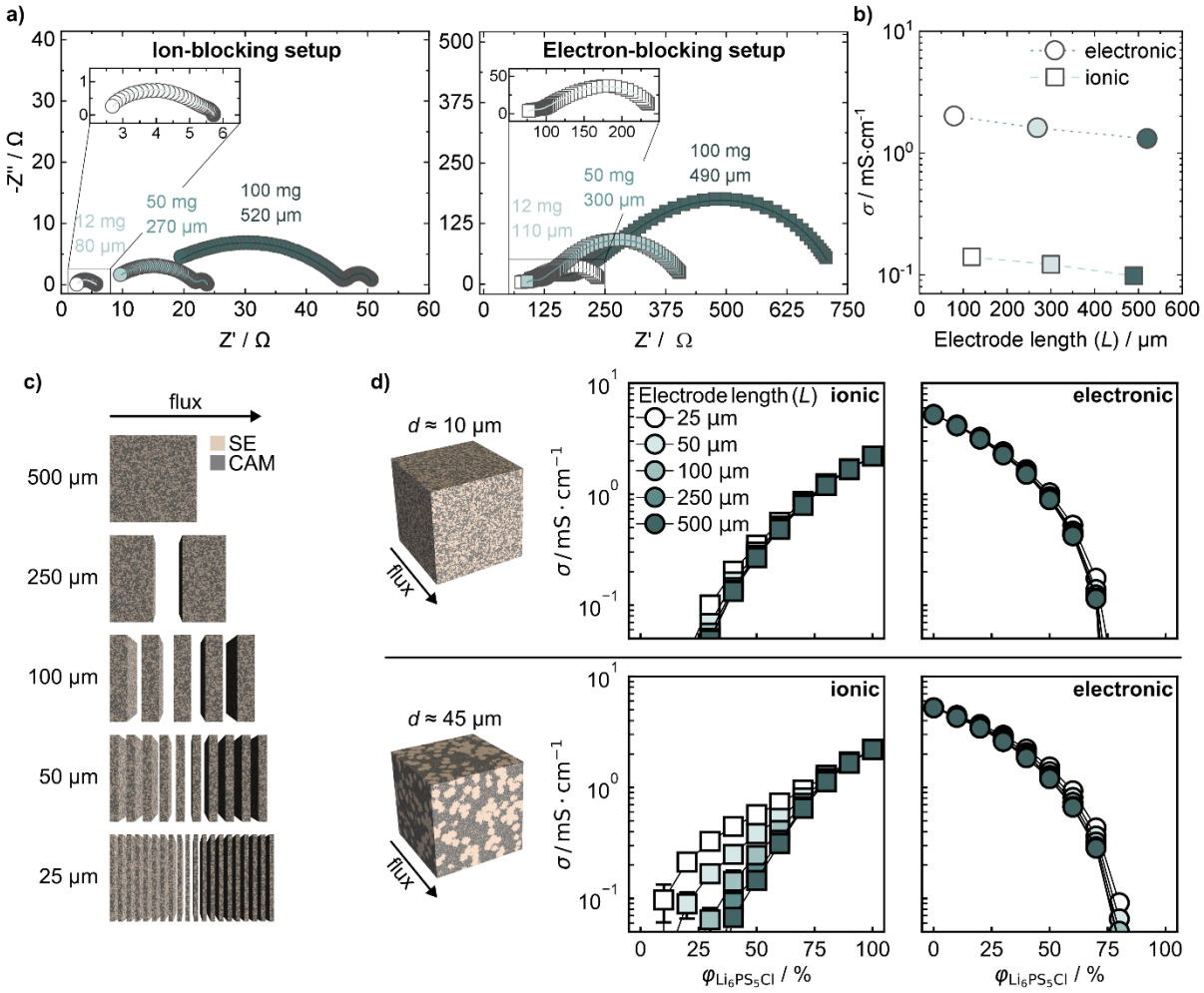

Figure 4: a) Nyquist plot showing the ion-blocking and electron-blocking spectra taken at three different positive electrode composite thicknesses, b) thickness-dependence of the effective conductivities. All spectra were obtained with a CC with the CAM:SE volume ratio of 48:52. σ_{el} is obtained from the ion-blocking and σ_{ion} from the electron-blocking spectrum, each by fitting with the TLM *advanced*$_{el}$. c) Virtual microstructures of different lengths representing composites with equal volume fractions of SE and CAM. The average SE particle diameter corresponds to $d \approx 10$ µm. d) Simulated ionic and electronic conductivities for composites with various SE volume fractions, particle sizes and electrode lengths. The data shown correspond to the mean conductivities over all simulated electrodes, whereas the error bars represent the simple standard deviations.

The overall shape of the impedance spectra is consistent across all layer thicknesses (Figure 4a). However, halving the thickness results in more than a halving of the total resistance, regardless of whether the measurements were conducted under ion- or electron-blocking conditions. Therefore, we quantify a decrease of partial conductivities as the thickness of the composite electrodes increases.

(Figure 4b). To understand the latter trend, simulations on virtual electrode structures (Figure S4) have been performed. A resistor network model is utilized to study effective conductivities,[27] while random walk simulations are performed with *pytrax*[30] to study the tortuosities of the respective ionic and electronic pathways (Figure S5). In the first step, binary virtual microstructures consisting of SE and CAM are constructed as described previously.[27] Both, the volume fraction (φ_{SE}) and mean particle size (d) of the SE phase are varied in the composites to systematically investigate the influence of microstructure on transport. Each microstructure is subsequently divided into thinner equally sized electrodes (Figure 4c) to enable analysis of transport as a function of electrode length (L). In the resistor network simulations, the SE phase is set to be purely ion-conducting with σ_{ion} = 2.2 mS·cm^{-1} (ionic conductivity of Li_6PS_5Cl measured in this work), while the CAM phase is set purely electron-conducting with σ_e = 5.22 mS·cm^{-1} (electronic conductivity of NMC 83:6:11).[27] The computed $\sigma_{eff,el}$ and $\sigma_{eff,ion}$ are shown in Figure 4d as a function of SE volume fraction and electrode length (more simulated conductivities in Figure S6). Data are shown for virtual composites with a mean SE particle size of ≈ 10 µm (corresponding to the SE particle size determined in this work) and for composites incorporating larger SE particles of ≈ 45 µm.

Across all simulations, a rapid decrease in $\sigma_{eff,ion}$ and a corresponding increase in $\sigma_{eff,el}$ is observed with decreasing SE and increasing CAM volume fraction. The particle size trends in simulated conductivities of large structures (500 µm, typical for partial transport measurements) align well with literature reports and become increasingly more pronounced close to the percolation thresholds. In agreement with experimental findings by Schlautmann *et al.*,[5] the $\sigma_{eff,ion}$ decreases when the size of the SE particles in an electrode composite is increased from ≈ 10 µm to ≈ 45 µm. Conversely, the use of larger SE particles leads to higher $\sigma_{eff,el}$ of the composites, since a continuous conducting phase is less tortuous when large blocking particles are introduced than when the same volume fraction but smaller particles are used.[37]

In agreement with the experimental findings of this work, higher partial conductivities are observed when thinner electrodes are considered. This behavior can be attributed to the decreased tortuosity of the respective carrier pathways in thinner electrodes (Figure S5). As with the particle size trends, the effects of different electrode thicknesses are amplified when compositions close to the percolation thresholds are considered. Further, these differences are much more significant when large SE particles are used compared to small particles. The dependence of transport on electrode length shows up more drastically in the ionic conductivity than in the electronic conductivity trends. This is because the particle sizes of the ion-conducting phases were explicitly varied throughout the simulation series while the continuous electron-conducting phase only changed as a consequence when constructing the virtual microstructures. The observed length dependence of the transport properties can be attributed to finite size effects, that come into play when the investigated system size of a random composite is smaller than the representative volume element.[38,39] Finite size effects become increasingly more pronounced, when the ratio of obstacle size (*e.g.* electronically isolating SE particle) to system size increases.[40,41] This explains the larger differences in transport behavior with layer thickness when larger particles are used compared to smaller particles.

In summary, finite size effects can become relevant in electrode composites. Particularly when large particles (> 10 µm) are used, the conductivities determined in a transport measurement (≈ 500 µm) can differ significantly from those relevant in practical electrodes (≈ 50 µm). In such cases, electrode thickness must be considered to get a complete understanding of the overall transport behavior.

Time-, Pressure- and Temperature-dependence of Partial Transport

We evaluated the temporal evolution of the CC to attain a better understanding of interfacial phenomena between the CAM and the SE phases. Similar studies have been conducted before and report a net increase in the total resistance of the cells but with different magnitudes and explanations: either mechanical relaxation[42] of the cell and its components after cell assembly or chemical degradation reactions between the CAM and the LPSCl SE, supported by XPS

measurements.[26] Due to the (electro)chemical instability of the LPSCl SE against oxide-based CAMs,[43–45] we expect that the total resistance of the CC increases over time. However, unlike previous studies, we conducted these experiments in ion- and electron-blocking configurations to quantify via TLM fits to the impedance spectra which of the components is contributing the most to the resistance increase. For both ion- and electron-blocking cells, an increase in the total impedance is observed over time, but the absolute resistances obtained are different (Figure 5). Using the *advanced*$_{el}$ TLM model, we quantified all resistances and observe that they all scale linearly against $t^{1/2}$ for both the ion-blocking (Figure 5a) and electron-blocking (Figure 5b) setups, suggesting a chemical degradation process.[26] The linear fits are depicted in Figure 5c, the slopes from the linear regression are shown in Table ST2. The slope of the resistance increase k, also referred to as growth rates, is the highest for R_{ion} (7 $\Omega \cdot h^{-0.5}$, determined from the electron-blocking measurement), and lower for the total R_{el} (3 $\Omega \cdot h^{-0.5}$, determined from the ion-blocking measurement), mainly due to the increase in $R_{el,int}$ (in the same range as k for R_{el}), whereas almost no change is observed for $R_{el,bulk}$ (0.1 $\Omega \cdot h^{-0.5}$) over time. Comparing the results from the two different measurement setups (Figure S7), the trend in the slopes is the same in both measurements, validating the measurement. However, the slopes are always higher when determined from the "wrong" measurement setup. In contrast, the relative increase (Figure S8) of each R_{ion} and R_{el} over time is similar regardless of the measurement setup. The results indicate a decrease of both the electronic and ionic conductivity over time, for the electronic conductivity this is due the increase of interfacial resistance ($R_{el,int}$), suggesting a chemical degradation reaction at the NMC interface. The growth rates (k) we quantify here are in the same order of those reported for solid-state battery half-cells that contain Zn-doped chloride-rich lithium argyrodite as a catholyte with $LiNi_{0.83}Co_{0.11}Mn_{0.06}O_2$ as CAM and held at a potential of 3.5 V *vs.* $Li^+|Li$.[46] The latter suggests that, even at 0% SOC, the LPSCl and NMC are not chemically stable and the formation of degradation products and/or the cathode electrolyte interface (CEI) already ensues prior to cycling. The latter has strong implications when considering the storage of prepared composite electrodes and the long-term storage of uncycled solid-state battery cells.

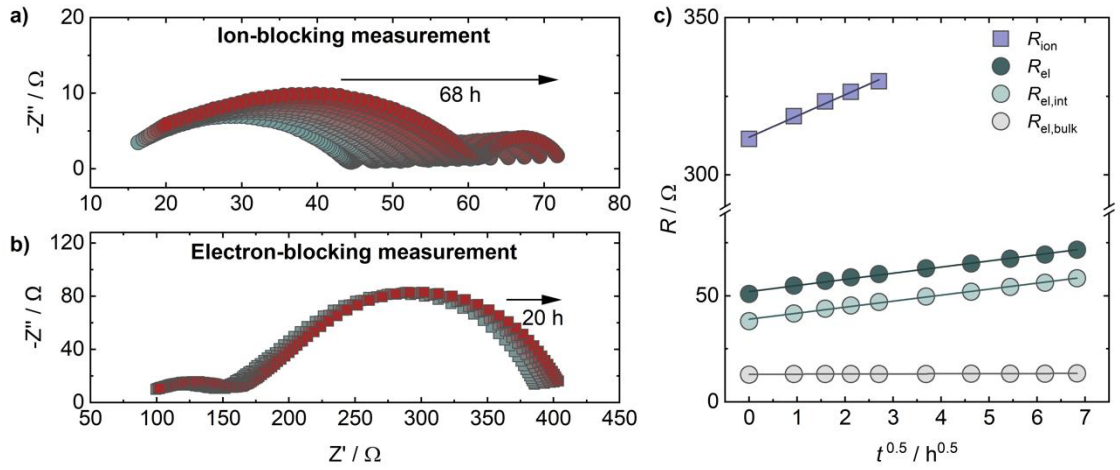

Figure 5: Evolution of a) the impedance of an ion-blocking cell over 68 h at 25 °C and b) the impedance of an electron-blocking cell over 20 h at 25 °C. c) Electronic and ionic resistances, obtained from the fits of the ion-blocking and electron-blocking measurements, respectively. The resistances are plotted versus the square root of time and show a linear behavior with R^2 values > 0.99. The composite positive electrode with a CAM:SE volume ratio of 48:52 and thickness of ≈500 µm was used in the measurements.

To investigate the hypothesis of mechanical relaxation as a cause for the observed increase in the resistances, we studied the influence of the applied pressure during measurement (stack pressure) on the resulting impedance spectra of ion-blocking cells. In the measurement performed under controlled pressure, the impedance was measured after initial compression (380 MPa) at a stack pressure of 50 MPa. Then, the stack pressure was lowered in steps of 10 MPa down to 10 MPa, and an impedance spectrum was measured at each pressure step (Figure 6a). In general, we expect an increase in the resistances as the stack pressure is reduced, and we quantify this trend in Figure 6b using the calculated partial conductivities. These results emphasize the importance of sustained interparticle contact (in this case via applied stack pressure) to enable the transport of ions and electrons in composite electrodes, as well as to maintain contact with the stainless-steel electrode. Interestingly, upon repressing the CC to the initial stack pressure of 50 MPa, the resistances do not return to the initial values, but rather to higher values, resulting in a net lowering of 38% for $\sigma_{eff,el}$ and 45% for $\sigma_{eff,ion}$. These results confirm the existence of mechanical relaxation and its effect on the partial transport in composite electrodes. To understand this behavior, one must consider the expected

processes during powder compression. In general, powder compression can be divided into three phases. Initially, particle rearrangement takes place, accompanied by local elastic deformations. This is followed by a regime where plastic deformations come into play, along with elastic contributions. At very high pressures, the whole pellet behaves elastically. For the sulfide-based SE *t*-Li_7SiPS_8, plastic deformations starts at around 500 MPa.[47] Similar measurements for LPSCl show plastic deformations above ≈100 MPa, depending on the SE particle size.[48] Upon pressure release, spring back behavior and elastic recovery cause pellet relaxation by an increase of the pellet thickness, which is accompanied by a density decrease and reduction of the ionic conductivity.[47] This spring back is likely one cause for the observed reduction of effective conductivities in CCs after readjusting the stack pressure. As the Young modulus of LPSCl (22.1 GPa)[49] is much lower compared to the one of NMC (above 150 GPa, depending on the determination method and composition),[50] the latter is expected to be deformed less under the applied pressure. An immediate conclusion from these results is that opening cells to modify the measurement setup for a specific CC sample is not a reliable approach. For example, converting a sample characterized in an ion-blocking cell after some rest time and impedance measurement to an electron-blocking by opening it, adding two SE and two In/$(InLi)_x$ layers on each side and repressing,[9] will lead to a different partial transport in the composite electrode and an incomparable measurement because of the sample history. Note that it is unlikely that the temporal behavior in Figure 5 is solely originating from the mechanical relaxation effect because the timescales studied are very different, namely the pressure-dependent measurements reported here encompass less than an hour of total measurement time in the stack pressure range studied. Therefore, the most likely explanation of the time-dependent increase in the resistances of CC is chemical degradation, and we have been able to pinpoint the formation of a new interphase on the CAM as the most likely cause based on our TLM analysis of the impedance spectra.

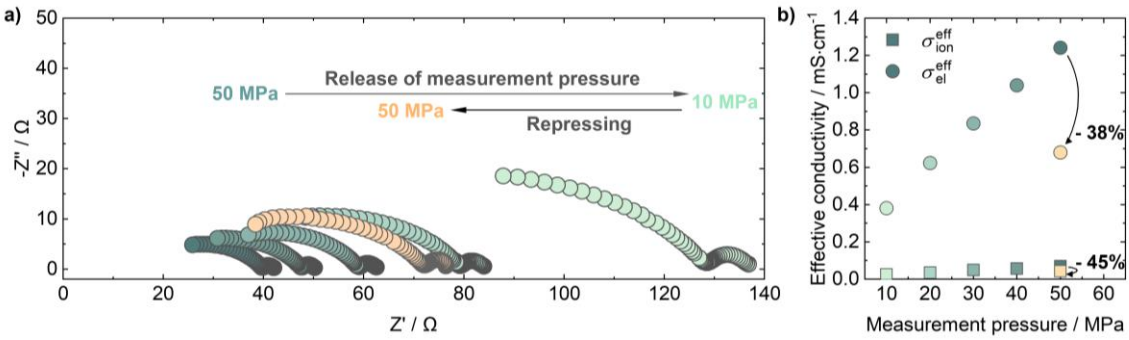

Figure 6: Ion-blocking impedance measurements of the CC (CAM:SE 48:52 vol%) performed under controlled pressure. a) Nyquist plots as a function of stack pressure. Here, the stack pressure was lowered from 50 MPa initially to 10 MPa in steps of 10 MPa. Afterwards, one more measurement was performed at 50 MPa (repressing). b) Calculated partial conductivities obtained from the TLM *advanced*$_{el}$ model. The percentages shown state the change of the conductivity after the repressing step to 50 MPa. The thickness of the pellet was 590 µm after the measurement.

As heating steps may be required during processing or cycling of composite positive electrodes, the influence of stepwise heating on the partial conductivities of CCs was investigated. Here, the impedance spectra of symmetric ion- and electron-blocking cells were measured at 25 °C, 40 °C and 60 °C during heating and at 40 °C and 25 °C during cooling, after 2 h of equilibration time at each temperature step. Figure 7 shows the temperature-dependent impedance spectra of the CC with the 48:52 vol% NMC 83:6:11:Li_6PS_5Cl ratio (in the following referred to as reference sample) measured in an ion- and electron-blocking measurement setup, and their corresponding Arrhenius plots. As expected, the impedance spectra measured at 60 °C show reduced high-, mid- and low-frequency intercepts for both the ion- and electron-blocking setup. However, a drastic change of the spectra is visible after cooling the cells back to the initial temperature of 25 °C.

In the following, we discuss the evolution of the ion-blocking spectrum (Figure 7a). After cooling back to 25 °C, the low-frequency intercept $R_{2,el}$ (equal to R_{el}) and the mid-frequency intercept $R_{1,el}$ are at higher resistances compared to the initial values. This increase in resistance after heating corresponds to a decrease in $\sigma_{eff,el}$, which is depicted in the Arrhenius plot in Figure 7b. As a result, different activation energies ($E_{a,el}$) are determined during heating and cooling, *i.e.* lower activation energies are

observed during heating, and higher ones are observed during cooling. To exclude that this observed effect is due to pressure changes caused by cell deformations during heating of the cell casing, frame and stamps, a reference temperature-dependent measurement was performed at fixed pressure (Figure S9). The trends in activation energies under these controlled conditions are consistent with those obtained from press cells. To investigate whether this effect is related to interfacial decomposition reactions, we repeated the ion-blocking measurement with another material combination. When $LiNi_{0.6}Mn_{0.2}Co_{0.2}O_2$ (NMC 622) is used instead of NMC 83:6:11, a lower total electronic conductivity and a much less pronounced decrease in $\sigma_{eff,el}$ of only 6% (Figure S10) is observed after the heating step. The lower $\sigma_{eff,el}$ is explained by the lower electronic conductivity of pure NMC 622 compared to NMC 83:6:11.[51–53] The activation energies of the CCs, extracted during heating, are 0.08 eV for the NMC 83:6:11- and 0.19 eV for the NMC 622-based CC, respectively. The former value deviates significantly from the literature activation energy, which is 0.24 eV for pure NMC 811 and 0.27 eV for pure NMC 622.[51] During cooling, the determined $E_{a,el}$ for NMC 622 is with 0.20 eV almost the same as during heating, whereas a largely increased $E_{a,el}$ of 0.22 eV is observed during cooling for NMC 83:6:11. The less significant decrease in $\sigma_{eff,el}$ of only 6% for the NMC 622-based CC and the smaller difference between the $E_{a,el}$ between heating and cooling might be related to the different chemical stability of thiophosphate-based SE against the NMCs, as the chemical stability is known to decrease with higher Ni contents.[54,55] These results indicate that (changes in) the CAM is the determining factor that causes the resistance increase upon heating.

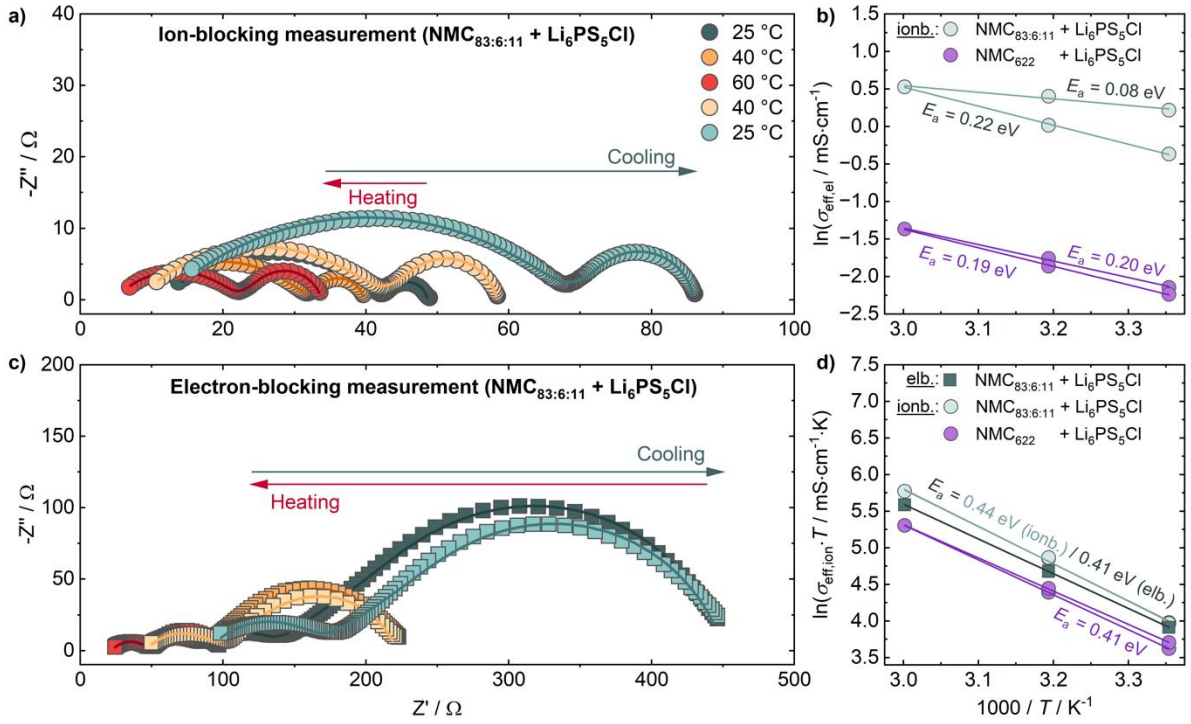

Figure 7: a) Temperature-dependent impedance spectra of an ion-blocking cell with a CAM:SE ratio of 48:52 vol% during heating from 25°C to 60 °C and cooling back to 25 °C, b) Arrhenius plot showing the temperature-dependent electronic conductivities obtained from the fitting of the ion-blocking (ionb.) spectra for three different composite electrodes and the activation energies, c) the temperature dependent impedance spectra of an electron blocking cell with 48:52 CAM:SE vol% ratio and d) Arrhenius plot depicting the temperature-dependence of the ionic conductivities. Note that for the ionic conductivities in d), only the reference composite (NMC 83:6:11 and Li_6PS_5Cl) was measured in an electron-blocking (elb.) cell, the other conductivities are derived from the ion-blocking (ionb.) measurement. Each PEIS measurement was performed at a frame pressure of 50 MPa, the CC thickness was each ≈500 µm.

Regarding the electron-blocking setup (Figure 7c), only a slight increase is observed in the low-frequency intercept $R_{2,ion}$ (equal to R_{ion}+R_{SE}+$R_{SE|In/(InLi)x}$; for the temperature-dependent determination of R_{SE} and $R_{SE|In/(InLi)x}$, see Figure S11) after the heating step. That means similar ionic conductivities are measured before and after heating, and similar $E_{a,ion}$ are measured irrespective if they are determined from heating or cooling (Figure 7d). Conversely, a large increase is observed for the mid-frequency intercept $R_{1,ion}$ after heating, which is in accordance with the increase of $R_{1,el}$ in the electron-blocking setup. In Figure 7d, the conductivities obtained from the ion- and electron-blocking NMC 83:6:11:LPSCl measurement show good agreement. Thus, the temperature-dependent $\sigma_{eff,ion}$ of

590 the NMC 622:LPSCl CC was extracted from the ion-blocking cell for a rough estimate without the
591 preparation of an additional electron-blocking cell. The CC prepared with NMC 622 shows a slightly
592 lower ionic conductivity compared to the CC with NMC 83:6:11, maybe due to particle size changes or
593 the measurement errors. The $E_{a,ion}$ of all samples are similar, ranging from 0.38 eV to 0.44 eV, which
594 is slightly higher than what is reported for pure Li_6PS_5Cl (0.33 eV).[56] No large difference is observed
595 between heating and cooling.
596 The results show that a decrease in the electronic conductivity is observed after heating the CC to
597 60 °C, without large changes in the ionic conductivity. This could be related to a surface change or
598 decomposition primarily affecting the CAM (surface), similar to the observed effect of the increase of
599 $\sigma_{eff,el}$ over time, which was shown in Figure 5. However, unlike the time-dependent change, minimal
600 changes are observed for $\sigma_{eff,ion}$, suggesting that a different degradation mechanism is taking place.
601 Although the same behavior was observed under controlled pressure, the contribution of changes in
602 the contact resistance between the CC and the current collector cannot be completely excluded as a
603 contributing factor. Note that additionally, commercial NMCs are often coated and/or doped to
604 change the stability of the material against the LPSCl SE,[57] and/or possess residual surface lithium
605 impurities,[58] all of which can influence the temperature-dependent behavior of the CCs in different
606 ways.
607 Taken together, multiple changes occur after the preparation of CC at high pressures. Firstly, after
608 mixing CAM and LPSCl, a degradation process/reaction takes place which hinders the transport. A
609 constant linear resistance growth that scales with the square root of time is observed within the
610 timescale of our experiments. Secondly, mechanical relaxation of the composite electrodes is present
611 upon pressure release, which strongly influences the partial transport. This should be taken into
612 account when optimizing (large-scale) electrode preparation protocols. Lastly, temperature treatment
613 of the cathode composites leads to changes in the partial transport, presumably via a degradation
614 mechanism that is different from the one appearing over time and/or which exacerbates the
615 degradation of one component (the CAM) in the CC.

Influence of Partial Transport on Cycling Performance

Lastly, cycling experiments on the composites with the three different CAM:SE vol% ratios were performed, the specific discharge capacities and Coulomb efficiencies are depicted in Figure 8a and Figure 8b, respectively. The tests were conducted at 0.5C for 300 cycles in which the first seven cycles served as formation and pretreatment cycles in which lower rates were applied (0.05C, 0.05C, 0.1C, 0.05C, 0.1C and 0.2C). During these formation cycles, the 61:39 vol% CAM:SE ratio composite ($CC_{61:39}$) exhibits the highest specific capacities, whereas the specific capacities of the 48:52 vol% composite $CC_{48:52}$ and the 37:63 vol% composite $CC_{37:63}$ show lower specific capacities (Figure 8c). This capacity difference during the formation steps between the $CC_{61:39}$ and the composites containing smaller CAM contents is particularly pronounced at small C-rates (30 $mAh \cdot g^{-1}$ difference at initial 0.05C cycle). At cycles conducted with higher C-rates however, this difference is reduced significantly to *e.g.* 1 $mAh \cdot g^{-1}$ at the first 0.5C cycle.

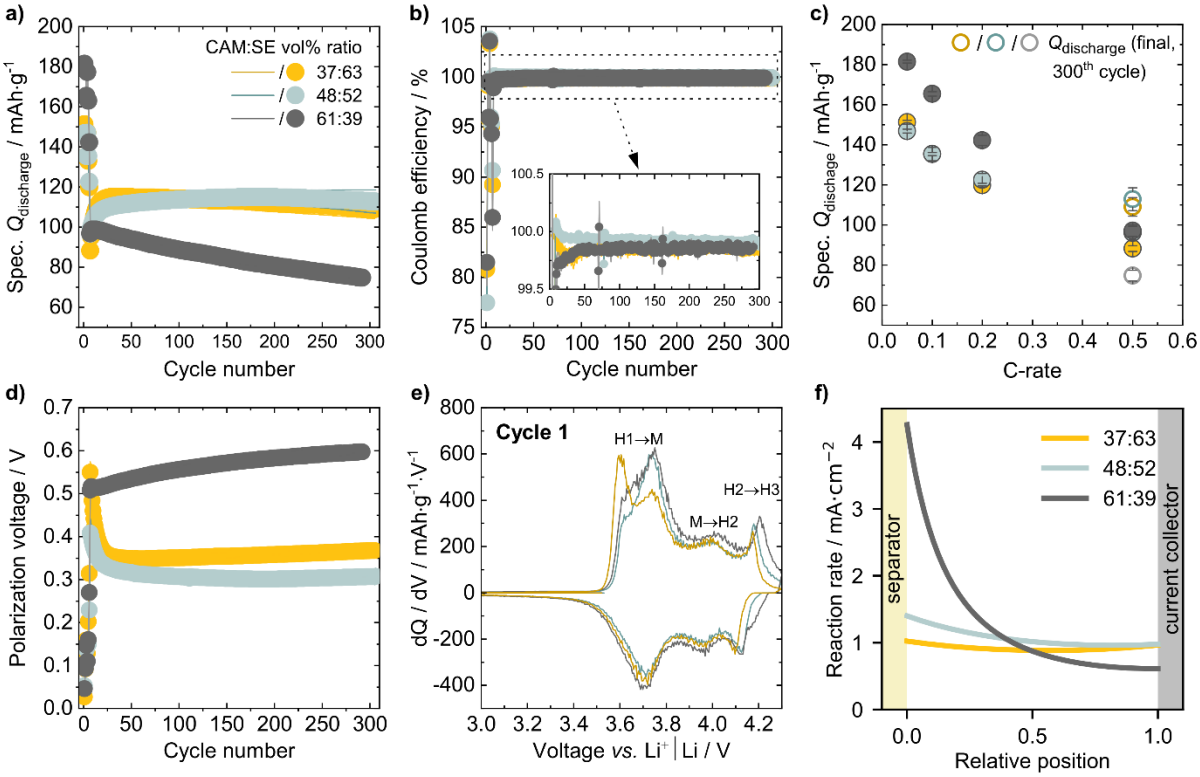

Figure 8: Cycling of positive electrode composites with different CAM:SE volume ratios. a) Specific discharge capacities during long-term cycling; b) Coulomb efficiencies; c) rate capability of each the first cycle at every C-rate during formation (filled circles) and the final C-rates at 0.5C (open circles), d) polarization voltages calculated from average charge minus average

discharge voltage. Cycling was performed in press cells at 0.5C and after a pretreatment of 0.05C, 0.05C, 0.1C, 0.05C, 0.1C and 0.2C with a cycling pressure of 50 MPa. Shown is the average and standard deviation of three cells. e) Differential capacity of the first and f) reaction rate distribution as a function of position in the cathode composite, calculated using porous electrode theory by Newman and Tobias.[59]

Despite $CC_{61:39}$ showing the highest capacities during the formation cycles, it shows the lowest capacity retention during 0.5C cycling. For all cells, an increase of the specific discharge capacity Q_{act} over cycling at 0.5C (in the following referred to as *activation behavior*) is observed in the first n_{act} cycles. This activation behavior is the least pronounced for $CC_{61:39}$ (Q_{act}= 2 mAh·g^{-1}, n_{act}= 11), and very evident for $CC_{37:63}$ (Q_{act}= 27 mAh·g^{-1}, n_{act}= 34) and $CC_{48:52}$ (Q_{act}= 18 mAh·g^{-1}, n_{act}= 182). The polarization voltage, calculated as the difference between the average charge and average discharge voltages, is consistent with these results, showing a decrease of the polarization at initial cycles for $CC_{48:52}$ and $CC_{37:63}$ where the activation behavior is observed (Figure 8d). The decrease in polarization indicates that the cell resistance is decreasing. Additionally, the Coulomb efficiencies (Figure 8b) in the first three and fourteen 0.5C cycles for the cells $CC_{37:63}$ and $CC_{48:52}$ are over 100%, respectively, indicating that the capacity loss due to the high C-rate is partly recovered or that a decomposition reaction occurs. Three phase transitions are present in the differential capacity (dQ/dV) plot (Figure 8e): hexagonal to monoclinic (H1→M), monoclinic to hexagonal (M→H2) and another hexagonal phase transition (H2→H3).[60] For the H1→M transition, two peaks are present during charge, which is especially visible in the first cycle (0.05 C). The two peaks of the H1→M phase transition have different intensity ratios for the different compounds. For $CC_{37:63}$, there is an intense first peak at 3.60 V *vs.* $Li^+|Li$ and a suppressed second peak at 3.75 V *vs.* $Li^+|Li$, in contrast to a less intense first peak which is only observed as a shoulder, and a very intense second peak for the other two CCs which are richer in CAM. Another mayor difference is observed in the H2→H3 peak during charging. This transition is shifted to higher voltages, with higher CAM content, and is known to be responsible for anisotropic volume changes, leading to capacity fading,[61,62] the latter is observed here for higher CAM contents. These differences are still present in the second cycle (0.05C, Figure S12a), but they become less

pronounced. In further cycling, the activation behavior is accompanied by the intensification of the H2→H3 phase transition (Figure S12b).

Connecting the observed cycling performance to the measured partial transport, $CC_{61:39}$ with the highest CAM content shows the lowest effective ionic conductivity (0.033 $mS \cdot cm^{-1}$), the highest polarization voltages and the worst cycling stability. Thus, its partial ionic conductivity is not sufficient to enable high C-rates, leading to the high polarization voltages observed. On the other hand, $CC_{37:63}$ which has the lowest electronic conductivity (0.35 $mS \cdot cm^{-1}$) and $CC_{48:52}$ show similar cycling behavior, with slightly lower capacities during most of the cycling and a marginally worse rate capability for the former. These results indicate that for the investigated system, the partial ionic conductivity limits cycling performance and might lead to inhomogeneous reaction current distribution in the composite electrode, inducing reaction fronts.[63] To determine the distribution of the reaction rates in the CCs, additional simulations were performed. While *operando* measurements require complicated measurement setups, porous electrode theory by Newman and Tobias provides a quick tool to estimate the reaction rate distribution along an electrode based on the experimental parameters (details in Section 5 of the Supporting Information).[59] Although developed for porous electrodes filled with an electrolyte solution, it can also be applied to solid-state batteries, as the general boundary conditions remain the same.[64] The calculated reaction rates are shown in Figure 8f. Similar and relatively uniform reaction rate distributions are predicted for the composites $CC_{37:63}$ and $CC_{48:52}$, whereas $CC_{61:39}$ clearly shows inhomogeneous current distribution with significantly higher reaction rates near the separator. The pronounced reaction rate inhomogeneity in $CC_{61:39}$ arises from its limited ionic conductivity. In combination with its much higher electronic conductivity, this leads to electrode reactions predominantly occurring near the separator. With this, the model predicts larger reaction rate inhomogeneities when cycling $CC_{61:39}$, which could explain the faster capacity fading observed during long term cycling for this composition.

Interestingly, $CC_{37:63}$ which shows a $\sigma_{eff,ion}$:$\sigma_{eff,ion}$ ratio near 1 (measured in the thick electrode setup), does not show the best results in terms of polarization voltage and long-term cycling stability. Thus, there must be other factors beyond optimized partial transport at 0% SOC influencing the cycling performance, as already suggested by Hendriks *et al.*.[8] More recently, Kissel *et al.* introduced the terms *static capacity* and *dynamic capacity* to distinguish between two types of capacity losses with respect to the theoretical capacity of an electroactive material.[65] The *static capacity* is the capacity that remains after composite electrode preparation, and possible causes for losses are poor mixing, poor electrode design and electronic contact losses during cycling, all of which lead to inaccessible CAM particles (active mass loss). The *dynamic capacity* is defined as the remaining capacity after kinetic losses upon cycling. Such losses originate from poor transport properties, *e.g.* due to high tortuosities and/or low partial conductivities, interfacial degradation or partial contact losses during cycling, and become more evident at high C-rates.[65] As such, the quantification of the partial transport of CCs in (thick) symmetric cells has limited predictability with respect to the cycling performance of such CC in (half/full) battery cells. The limited transferability is, on the one hand, due to the finite size effects we identified and, on the other hand, due to fact that static and dynamic capacity losses are not accounted for at 0% SOC. Instead, we have been able to utilize such symmetric cell transport measurements to evaluate some of the contributors to static capacity losses (surface layer formation, decomposition products, pressure relaxation) that can lead to additional kinetic losses (e.g. lower partial transport and/or higher tortuosities) that influence the resulting dynamic capacity. Note that the microstructure and partial transport of the CC changes during cycling, due to the volumetric changes of the NMC particles during the (de)intercalation of lithium ions, especially for higher Ni contents,[66,67] and the increase of electronic conductivity of CAMs during deintercalation.[51–53] Moreover, finite size effects on the partial transport occurring in thin electrodes, interfacial degradation and the possibility of reaction fronts, all of which were quantified in this study, are specific examples of how poor transport properties contribute to kinetic losses, causing the resulting dynamic capacities of the CCs.

Conclusion

In conclusion, the present study discusses the usage of TLMs to determine partial transport in positive composite electrodes. In the first part, three different TLMs and their corresponding impedance response in Nyquist plots are shown. By varying the CAM:SE ratio, the TLM that accounts for an interparticle resistance between the CAM particles showed the most physically reasonable fits. The impedance spectra change over time, mainly due to a large increase in $R_{el,int}$ and a slighter one in R_{ion}, suggesting a chemical degradation process at the surface of the CAM that primarily impedes the transport of electrons in the CC. Similarly, an increase in R_{el} after heating to 60 °C was observed, strongly dependent on the used NMC species. With respect to the preparation of symmetric cells to quantify partial transport, future reports should be careful about opening and reclosing a prepared cell, as the partial conductivities change due to mechanical relaxation. Additionally, partial conductivities and tortuosity can vary with the thickness of a composite electrode. Specifically, the partial transport of a given CC measured in a thick configuration differs from that one of a thinner electrode with the same composition, with a decrease in electrode thickness being accompanied by an increase in both ionic and electronic conductivity. Our simulations highlight that these finite size effects become particularly pronounced when large particles are used. Therefore, additional *ex-situ* measurements like scanning electron microscopy or *X*-ray tomography measurements are required to investigate the actual microstructure of the CC. At the minimum, the measurement of the particle size distribution should be performed to enable the evaluation of finite size effects when comparing the component's particle sizes with the thickness of the composite electrode.

Taken together, comprehensive pressure-, temperature- and time-dependent impedance studies on such symmetric cells at 0% SOC and the subsequent fitting with TLMs can provide deep insights on the compatibility of the CC components, possible degradation mechanisms as well as the expected initial static capacity of such CCs in cells, and they can help to reduce the effects of kinetic losses by optimizing the tortuosities. However, the transferability of the transport properties of such thick electrodes to battery cells is not straightforward and particularly limited by different aspects. Firstly,

734 inhomogeneous microstructures can show high partial conductivities, *e.g.* if both species are in
735 separate parts of the composite, but they will likely show large static and dynamic capacity losses
736 during cycling due to the inactive and/or inaccessible CAM particles. Therefore, (in-situ) OCP
737 relaxation should be used to quantify the CAM utilization and active mass loss during cycling.[65,68]
738 Secondly, the thickness-dependence of transport limits the transferability of the conductivities
739 measured in thick electrodes to thinner electrodes used for cycling due to finite size effects and
740 possible reaction fronts. Thirdly, the partial transport is changing over cycling, which is caused by
741 microstructural changes and the SOC-dependence of the partial electronic conductivity of CAM,
742 adding the necessity for *operando* and SOC-dependent quantification of the partial transport and
743 evolving microstructure. *Operando* quantifications in solid-state battery half-cells require the use of
744 Z-type TLM models with the same circuit elements in the electronic and ionic lines as the T-type model,
745 but with an ionic connection towards the separator and an electronic connection towards the current
746 collector.[17] However, charge-transfer resistances cannot be neglected and complicate the
747 interpretation of the impedance spectra. As such, more systematic studies are needed to evaluate,
748 understand and validate the implementation of TLM models to describe the impedance spectra of
749 solid-state battery cells. Despite these limitations, the detailed pressure-, temperature- and time-
750 dependent impedance studies on symmetric cells and the subsequent fitting with TLMs can provide
751 valuable insights on the compatibility of the CC components, possible degradation mechanisms as well
752 as the expected initial static capacity and factors leading to kinetic losses that aid the development of
753 composite electrodes for solid-state battery cells.

754 **Supporting Information**

755 Details on the transmission line models, numerical simulations, time- and temperature-dependent
756 partial transport, differential capacity plots, material characterization and details on the reaction rate
757 calculations using the Newman and Tobias model and additional references can be found in the
758 Supporting Information document.

759 **Acknowledgements**

760 The S.P. and N.M.V-B acknowledge the FESTBATT Cluster of Competence funded by the
761 Bundesministerium für Bildung und Forschung (BMBF; project 13XP0428A). L.K. is a member of the

International Graduate School for Battery Chemistry, Characterization, Analysis, Recycling and Application (BACCARA), funded by the Ministry for Culture and Science of North Rhine Westphalia, Germany.

References

(1) Janek, J.; Zeier, W. G. A solid future for battery development. *Nat. Energy* **2016**, *1* (9). DOI: 10.1038/nenergy.2016.141.

(2) Janek, J.; Zeier, W. G. Challenges in speeding up solid-state battery development. *Nat. Energy* **2023**, *8* (3), 230–240. DOI: 10.1038/s41560-023-01208-9.

(3) Nguyen, T.-T.; Demortière, A.; Fleutot, B.; Delobel, B.; Delacourt, C.; Cooper, S. J. The electrode tortuosity factor: why the conventional tortuosity factor is not well suited for quantifying transport in porous Li-ion battery electrodes and what to use instead. *Npj Comput. Mater.* **2020**, *6* (1). DOI: 10.1038/s41524-020-00386-4.

(4) Shi, T.; Tu, Q.; Tian, Y.; Xiao, Y.; Miara, L. J.; Kononova, O.; Ceder, G. High Active Material Loading in All-Solid-State Battery Electrode via Particle Size Optimization. *Adv. Energy Mater.* **2020**, *10* (1). DOI: 10.1002/aenm.201902881.

(5) Schlautmann, E.; Weiß, A.; Maus, O.; Ketter, L.; Rana, M.; Puls, S.; Nickel, V.; Gabbey, C.; Hartnig, C.; Bielefeld, A.; Zeier, W. G. Impact of the Solid Electrolyte Particle Size Distribution in Sulfide-Based Solid-State Battery Composites. *Adv. Energy Mater.* **2023**, *13* (41). DOI: 10.1002/aenm.202302309.

(6) Perrenot, P.; Bayle-Guillemaud, P.; Villevieille, C. Composite Electrode (LiNi0.6Mn0.2Co0.2O2) Engineering for Thiophosphate Solid-State Batteries: Morphological Evolution and Electrochemical Properties. *ACS Energy Lett.* **2023**, *8* (11), 4957–4965. DOI: 10.1021/acsenergylett.3c01975.

(7) Minnmann, P.; Schubert, J.; Kremer, S.; Rekers, R.; Burkhardt, S.; Ruess, R.; Bielefeld, A.; Richter, F. H.; Janek, J. Editors' Choice—Visualizing the Impact of the Composite Cathode Microstructure and Porosity on Solid-State Battery Performance. *J. Electrochem. Soc.* **2024**, *171* (6), 60514. DOI: 10.1149/1945-7111/ad510e.

(8) Hendriks, T. A.; Lange, M. A.; Kiens, E. M.; Baeumer, C.; Zeier, W. G. Balancing Partial Ionic and Electronic Transport for Optimized Cathode Utilization of High-Voltage LiMn2O4/Li3InCl6 Solid-State Batteries. *Batter. Supercaps* **2023**, *6* (4). DOI: 10.1002/batt.202200544.

(9) Minnmann, P.; Quillman, L.; Burkhardt, S.; Richter, F. H.; Janek, J. Editors' Choice—Quantifying the Impact of Charge Transport Bottlenecks in Composite Cathodes of All-Solid-State Batteries. *J. Electrochem. Soc.* **2021**, *168* (4), 40537. DOI: 10.1149/1945-7111/abf8d7.

(10) Asano, T.; Yubuchi, S.; Sakuda, A.; Hayashi, A.; Tatsumisago, M. Electronic and Ionic Conductivities of LiNi1/3Mn1/3Co1/3O2 -Li3PS4 Positive Composite Electrodes for All-Solid-State Lithium Batteries. *J. Electrochem. Soc.* **2017**, *164* (14), A3960-A3963. DOI: 10.1149/2.1501714jes.

(11) Dewald, G. F.; Ohno, S.; Hering, J. G. C.; Janek, J.; Zeier, W. G. Analysis of Charge Carrier Transport Toward Optimized Cathode Composites for All-Solid-State Li–S Batteries. *Batter. Supercaps* **2021**, *4* (1), 183–194. DOI: 10.1002/batt.202000194.

(12) Ohno, S.; Zeier, W. G. Toward Practical Solid-State Lithium–Sulfur Batteries: Challenges and Perspectives. *Acc. Mater. Res.* **2021**, *2* (10), 869–880. DOI: 10.1021/accountsmr.1c00116.

(13) Bisquert, J. Influence of the boundaries in the impedance of porous film electrodes. *Phys. Chem. Chem. Phys.* **2000**, *2* (18), 4185–4192. DOI: 10.1039/b001708f.

(14) Huang, J.; Gao, Y.; Luo, J.; Wang, S.; Li, C.; Chen, S.; Zhang, J. Editors' Choice—Review—Impedance Response of Porous Electrodes: Theoretical Framework, Physical Models and Applications. *J. Electrochem. Soc.* **2020**, *167* (16), 166503. DOI: 10.1149/1945-7111/abc655.

(15) Landesfeind, J.; Hattendorff, J.; Ehrl, A.; Wall, W. A.; Gasteiger, H. A. Tortuosity Determination of Battery Electrodes and Separators by Impedance Spectroscopy. *J. Electrochem. Soc.* **2016**, *163* (7), A1373-A1387. DOI: 10.1149/2.1141607jes.

(16) Morasch, R.; Keilhofer, J.; Gasteiger, H. A.; Suthar, B. Methods—Understanding Porous Electrode Impedance and the Implications for the Impedance Analysis of Li-Ion Battery Electrodes. *J. Electrochem. Soc.* **2021**, *168* (8), 80519. DOI: 10.1149/1945-7111/ac1892.

(17) Quemin, E.; Dugas, R.; Koç, T.; Hennequart, B.; Chometon, R.; Tarascon, J.-M. Decoupling Parasitic Reactions at the Positive Electrode Interfaces in Argyrodite-Based Systems. *ACS Appl. Mater. Interfaces* **2022**, *14* (43), 49284–49294. DOI: 10.1021/acsami.2c13150. Published Online: Oct. 20, 2022.

(18) Walther, F.; Randau, S.; Schneider, Y.; Sann, J.; Rohnke, M.; Richter, F. H.; Zeier, W. G.; Janek, J. Influence of Carbon Additives on the Decomposition Pathways in Cathodes of Lithium Thiophosphate-Based All-Solid-State Batteries. *Chem. Mater.* **2020**, *32* (14), 6123–6136. DOI: 10.1021/acs.chemmater.0c01825.

(19) Choi, W.; Ku, J. H.; Kim, Y.; Gwon, H.; Yoon, G.; Yu, D.; Kim, J.-S. Formulating Interfacial Impedances for Designing High-Energy and High-Power All-Solid-State Battery Cathodes. *ACS Appl. Mater. Interfaces* **2024**, *16* (20), 26066–26078. DOI: 10.1021/acsami.4c01322. Published Online: May. 13, 2024.

(20) Landesfeind, J.; Pritzl, D.; Gasteiger, H. A. An Analysis Protocol for Three-Electrode Li-Ion Battery Impedance Spectra: Part I. Analysis of a High-Voltage Positive Electrode. *J. Electrochem. Soc.* **2017**, *164* (7), A1773-A1783. DOI: 10.1149/2.0131709jes.

(21) Miß, V.; Ramanayagam, A.; Roling, B. Which Exchange Current Densities Can Be Achieved in Composite Cathodes of Bulk-Type All-Solid-State Batteries? A Comparative Case Study. *ACS Appl. Mater. Interfaces* **2022**, *14* (33), 38246–38254. DOI: 10.1021/acsami.2c06460. Published Online: Aug. 15, 2022.

(22) Schneider, L.; Klemens, J.; Herbst, E. C.; Müller, M.; Scharfer, P.; Schabel, W.; Bauer, W.; Ehrenberg, H. Transport Properties in Electrodes for Lithium-Ion Batteries: Comparison of Compact

versus Porous NCM Particles. *J. Electrochem. Soc.* **2022**, *169* (10), 100553. DOI: 10.1149/1945-7111/ac9c37.

(23) Wang, W.; Juarez-Robles, D.; Mukherjee, P. P. Electroanalytical Quantification of Electrolyte Transport Resistance in Porous Electrodes. *J. Electrochem. Soc.* **2020**, *167* (8), 80510. DOI: 10.1149/1945-7111/ab8975.

(24) Huggins, R. A. Simple method to determine electronic and ionic components of the conductivity in mixed conductors a review. *Ionics* **2002**, *8* (3-4), 300–313. DOI: 10.1007/BF02376083.

(25) Eckhardt, J. K.; Klar, P. J.; Janek, J.; Heiliger, C. Interplay of Dynamic Constriction and Interface Morphology between Reversible Metal Anode and Solid Electrolyte in Solid State Batteries. *ACS Appl. Mater. Interfaces* **2022**, *14* (31), 35545–35554. DOI: 10.1021/acsami.2c07077. Published Online: Jul. 25, 2022.

(26) Jung, S.-K.; Gwon, H.; Lee, S.-S.; Kim, H.; Lee, J. C.; Chung, J. G.; Park, S. Y.; Aihara, Y.; Im, D. Understanding the effects of chemical reactions at the cathode–electrolyte interface in sulfide based all-solid-state batteries. *J. Mater. Chem. A* **2019**, *7* (40), 22967–22976. DOI: 10.1039/c9ta08517c.

(27) Ketter, L.; Greb, N.; Bernges, T.; Zeier, W. G. Using resistor network models to predict the transport properties of solid-state battery composites. *Nat. Commun.* **2025**, *16* (1), 1411. DOI: 10.1038/s41467-025-56514-5. Published Online: Feb. 6, 2025.

(28) Santhosha, A. L.; Medenbach, L.; Buchheim, J. R.; Adelhelm, P. The Indium−Lithium Electrode in Solid-State Lithium-Ion Batteries: Phase Formation, Redox Potentials, and Interface Stability. *Batter. Supercaps* **2019**, *2* (6), 524–529. DOI: 10.1002/batt.201800149.

(29) Avila, L.; Ayachit, U., Eds. *The ParaView guide*:*Updated for ParaView version 4.3*, Full color version; Kitware Inc, 2015.

(30) Tranter, T. G.; Kok, M.; Lam, M.; Gostick, J. T. pytrax: A simple and efficient random walk implementation for calculating the directional tortuosity of images. *SoftwareX* **2019**, *10*, 100277. DOI: 10.1016/j.softx.2019.100277.

(31) Jamnik, J.; Maier, J. Treatment of the Impedance of Mixed Conductors Equivalent Circuit Model and Explicit Approximate Solutions. *J. Electrochem. Soc.* **1999**, *146* (11), 4183–4188. DOI: 10.1149/1.1392611.

(32) Nenning, A.; Opitz, A. Low oxygen partial pressure increases grain boundary ion conductivity in Gd-doped ceria thin films. *J. Phys. Energy* **2020**, *2* (1), 14002. DOI: 10.1088/2515-7655/ab3f10.

(33) Lai, W.; Haile, S. M. Impedance Spectroscopy as a Tool for Chemical and Electrochemical Analysis of Mixed Conductors: A Case Study of Ceria. *J. Am. Ceram. Soc.* **2005**, *88* (11), 2979–2997. DOI: 10.1111/j.1551-2916.2005.00740.x.

(34) Siroma, Z.; Fujiwara, N.; Yamazaki, S.; Asahi, M.; Nagai, T.; Ioroi, T. Mathematical solutions of comprehensive variations of a transmission-line model of the theoretical impedance of porous electrodes. *Electrochim. Acta* **2015**, *160*, 313–322. DOI: 10.1016/j.electacta.2015.02.065.

(35) Siroma, Z.; Sato, T.; Takeuchi, T.; Nagai, R.; Ota, A.; Ioroi, T. AC impedance analysis of ionic and electronic conductivities in electrode mixture layers for an all-solid-state lithium-ion battery. *J. Power Sources* **2016**, *316*, 215–223. DOI: 10.1016/j.jpowsour.2016.03.059.

(36) Ohno, S.; Bernges, T.; Buchheim, J.; Duchardt, M.; Hatz, A.-K.; Kraft, M. A.; Kwak, H.; Santhosha, A. L.; Liu, Z.; Minafra, N.; Tsuji, F.; Sakuda, A.; Schlem, R.; Xiong, S.; Zhang, Z.; Adelhelm, P.; Chen, H.; Hayashi, A.; Jung, Y. S.; Lotsch, B. V.; Roling, B.; Vargas-Barbosa, N. M.; Zeier, W. G. How Certain Are the Reported Ionic Conductivities of Thiophosphate-Based Solid Electrolytes? An Interlaboratory Study. *ACS Energy Lett.* **2020**, *5* (3), 910–915. DOI: 10.1021/acsenergylett.9b02764.

(37) Froboese, L.; van der Sichel, J. F.; Loellhoeffel, T.; Helmers, L.; Kwade, A. Effect of Microstructure on the Ionic Conductivity of an All Solid-State Battery Electrode. *J. Electrochem. Soc.* **2019**, *166* (2), A318-A328. DOI: 10.1149/2.0601902jes.

(38) Fathidoost, M.; Yang, Y.; Oechsner, M.; Xu, B.-X. Data-driven thermal and percolation analyses of 3D composite structures with interface resistance. *Mater. Des.* **2023**, *227*, 111746. DOI: 10.1016/j.matdes.2023.111746.

(39) Gitman, I. M.; Askes, H.; Sluys, L. J. Representative volume: Existence and size determination. *Eng. Fract. Mech.* **2007**, *74* (16), 2518–2534. DOI: 10.1016/j.engfracmech.2006.12.021.

(40) Astaneh, M.; Maggiolo, D.; Ström, H. Finite-size effects on heat and mass transfer in porous electrodes. *Int. J. Therm. Sci.* **2022**, *179*, 107610. DOI: 10.1016/j.ijthermalsci.2022.107610.

(41) Ghanbarian, B. Scale dependence of tortuosity and diffusion: Finite-size scaling analysis. *J. Contam. Hydrol.* **2022**, *245*, 103953. DOI: 10.1016/j.jconhyd.2022.103953. Published Online: Jan. 5, 2022.

(42) Koerver, R.; Aygün, I.; Leichtweiß, T.; Dietrich, C.; Zhang, W.; Binder, J. O.; Hartmann, P.; Zeier, W. G.; Janek, J. Capacity Fade in Solid-State Batteries: Interphase Formation and Chemomechanical Processes in Nickel-Rich Layered Oxide Cathodes and Lithium Thiophosphate Solid Electrolytes. *Chem. Mater.* **2017**, *29* (13), 5574–5582. DOI: 10.1021/acs.chemmater.7b00931.

(43) Schwietert, T. K.; Arszelewska, V. A.; Wang, C.; Yu, C.; Vasileiadis, A.; Klerk, N. J. J. de; Hageman, J.; Hupfer, T.; Kerkamm, I.; Xu, Y.; van der Maas, E.; Kelder, E. M.; Ganapathy, S.; Wagemaker, M. Clarifying the relationship between redox activity and electrochemical stability in solid electrolytes. *Nat. Mater.* **2020**, *19* (4), 428–435. DOI: 10.1038/s41563-019-0576-0. Published Online: Jan. 13, 2020.

(44) Tan, D. H. S.; Wu, E. A.; Nguyen, H.; Chen, Z.; Marple, M. A. T.; Doux, J.-M.; Wang, X.; Yang, H.; Banerjee, A.; Meng, Y. S. Elucidating Reversible Electrochemical Redox of Li6PS5Cl Solid Electrolyte. *ACS Energy Lett.* **2019**, *4* (10), 2418–2427. DOI: 10.1021/acsenergylett.9b01693.

(45) Dewald, G. F.; Ohno, S.; Kraft, M. A.; Koerver, R.; Till, P.; Vargas-Barbosa, N. M.; Janek, J.; Zeier, W. G. Experimental Assessment of the Practical Oxidative Stability of Lithium Thiophosphate Solid Electrolytes. *Chem. Mater.* **2019**, *31* (20), 8328–8337. DOI: 10.1021/acs.chemmater.9b01550.

(46) Hartel, J.; Banik, A.; Ali, M. Y.; Helm, B.; Strotmann, K.; Faka, V.; Maus, O.; Li, C.; Wiggers, H.; Zeier, W. G. Investigating the Influence of Transition Metal Substitution in Lithium Argyrodites on Structure, Transport, and Solid-State Battery Performance. *Chem. Mater.* **2024**, *36* (21), 10731–10745. DOI: 10.1021/acs.chemmater.4c02281.

(47) Schneider, C.; Schmidt, C. P.; Neumann, A.; Clausnitzer, M.; Sadowski, M.; Harm, S.; Meier, C.; Danner, T.; Albe, K.; Latz, A.; Wall, W. A.; Lotsch, B. V. Effect of Particle Size and Pressure on the Transport Properties of the Fast Ion Conductor t-Li7SiPS8. *Adv. Energy Mater.* **2023**, *13* (15). DOI: 10.1002/aenm.202203873.

(48) Lee, S.-Y.; Han, J.-H.; Gong, H.-W.; Ahn, J.; Yi, K.-W.; Cho, Y. W. Characterization of densification behavior and mechanical properties of solid electrolyte powders for all solid-state batteries. *J. Mater. Chem. A* **2025**, *13* (9), 6342–6346. DOI: 10.1039/D4TA08604J.

(49) Deng, Z.; Wang, Z.; Chu, I.-H.; Luo, J.; Ong, S. P. Elastic Properties of Alkali Superionic Conductor Electrolytes from First Principles Calculations. *J. Electrochem. Soc.* **2016**, *163* (2), A67-A74. DOI: 10.1149/2.0061602jes.

(50) Sun, H.; Zhao, K. Electronic Structure and Comparative Properties of LiNixMnyCozO2 Cathode Materials. *J. Phys. Chem. C* **2017**, *121* (11), 6002–6010. DOI: 10.1021/acs.jpcc.7b00810.

(51) Wang, S.; Yan, M.; Li, Y.; Vinado, C.; Yang, J. Separating electronic and ionic conductivity in mix-conducting layered lithium transition-metal oxides. *J. Power Sources* **2018**, *393*, 75–82. DOI: 10.1016/j.jpowsour.2018.05.005.

(52) Quemin, E.; Dugas, R.; Chaupatnaik, A.; Rousse, G.; Chometon, R.; Hennequart, B.; Tarascon, J.-M. An Advanced Cell for Measuring In Situ Electronic Conductivity Evolutions in All-Solid-State Battery Composites. *Adv. Energy Mater.* **2023**, *13* (31). DOI: 10.1002/aenm.202301105.

(53) Amin, R.; Chiang, Y.-M. Characterization of Electronic and Ionic Transport in Li1-xNi0.33Mn0.33Co0.33O2 (NMC 333) and Li1-xNi0.50Mn0.20Co0.30O2 (NMC 523) as a Function of Li Content. *J. Electrochem. Soc.* **2016**, *163* (8), A1512-A1517. DOI: 10.1149/2.0131608jes.

(54) Komatsu, H.; Banerjee, S.; Holekevi Chandrappa, M. L.; Qi, J.; Radhakrishnan, B.; Kuwata, S.; Sakamoto, K.; Ong, S. P. Interfacial Stability of Layered LiNixMnyCo1-x-yO2 Cathodes with Sulfide Solid

931 Electrolytes in All-Solid-State Rechargeable Lithium-Ion Batteries from First-Principles Calculations. *J.*
932 *Phys. Chem. C* **2022**, *126* (41), 17482–17489. DOI: 10.1021/acs.jpcc.2c05336.
933 (55) Wu, Y.-T.; Tsai, P.-C. Ab initio Interfacial Chemical Stability of Argyrodite Sulfide Electrolytes and
934 Layered-Structure Cathodes in Solid-State Lithium Batteries. *JOM* **2022**, *74* (12), 4664–4671. DOI:
935 10.1007/s11837-022-05472-0.
936 (56) Boulineau, S.; Courty, M.; Tarascon, J.-M.; Viallet, V. Mechanochemical synthesis of Li-argyrodite
937 Li6PS5X (X=Cl, Br, I) as sulfur-based solid electrolytes for all solid state batteries application. *Solid State*
938 *Ion.* **2012**, *221*, 1–5. DOI: 10.1016/j.ssi.2012.06.008.
939 (57) Walther, F.; Strauss, F.; Wu, X.; Mogwitz, B.; Hertle, J.; Sann, J.; Rohnke, M.; Brezesinski, T.; Janek,
940 J. The Working Principle of a Li2CO3/LiNbO3 Coating on NCM for Thiophosphate-Based All-Solid-State
941 Batteries. *Chem. Mater.* **2021**, *33* (6), 2110–2125. DOI: 10.1021/acs.chemmater.0c04660.
942 (58) Deng, S.; Sun, Q.; Li, M.; Adair, K.; Yu, C.; Li, J.; Li, W.; Fu, J.; Li, X.; Li, R.; Hu, Y.; Chen, N.; Huang,
943 H.; Zhang, L.; Zhao, S.; Lu, S.; Sun, X. Insight into cathode surface to boost the performance of solid-
944 state batteries. *Energy Storage Mater.* **2021**, *35*, 661–668. DOI: 10.1016/j.ensm.2020.12.003.
945 (59) Newman, J. S.; Tobias, C. W. Theoretical Analysis of Current Distribution in Porous Electrodes. *J.*
946 *Electrochem. Soc.* **1962**, *109* (12), 1183. DOI: 10.1149/1.2425269.
947 (60) Noh, H.-J.; Youn, S.; Yoon, C. S.; Sun, Y.-K. Comparison of the structural and electrochemical
948 properties of layered Li[NixCoyMnz]O2 (x = 1/3, 0.5, 0.6, 0.7, 0.8 and 0.85) cathode material for
949 lithium-ion batteries. *J. Power Sources* **2013**, *233*, 121–130. DOI: 10.1016/j.jpowsour.2013.01.063.
950 (61) Ryu, H.-H.; Namkoong, B.; Kim, J.-H.; Belharouak, I.; Yoon, C. S.; Sun, Y.-K. Capacity Fading
951 Mechanisms in Ni-Rich Single-Crystal NCM Cathodes. *ACS Energy Lett.* **2021**, *6* (8), 2726–2734. DOI:
952 10.1021/acsenergylett.1c01089.
953 (62) Ryu, H.-H.; Park, K.-J.; Yoon, C. S.; Sun, Y.-K. Capacity Fading of Ni-Rich Li[NixCoyMn1-x-y]O2 (0.6
954 ≤ x ≤ 0.95) Cathodes for High-Energy-Density Lithium-Ion Batteries: Bulk or Surface Degradation?
955 *Chem. Mater.* **2018**, *30* (3), 1155–1163. DOI: 10.1021/acs.chemmater.7b05269.
956 (63) Bradbury, R.; Dewald, G. F.; Kraft, M. A.; Arlt, T.; Kardjilov, N.; Janek, J.; Manke, I.; Zeier, W. G.;
957 Ohno, S. Visualizing Reaction Fronts and Transport Limitations in Solid-State Li–S Batteries via
958 Operando Neutron Imaging. *Adv. Energy Mater.* **2023**, *13* (17). DOI: 10.1002/aenm.202203426.
959 (64) Bernges, T.; Ketter, L.; Helm, B.; Kraft, M. A.; See, K. A.; Zeier, W. G. Transport characterization of
960 solid-state Li2FeS2 cathodes from a porous electrode theory perspective. *EES Batteries* **2025**, *1* (1),
961 172–184. DOI: 10.1039/d4eb00005f.
962 (65) Kissel, M.; Schosland, M.; Töws, J.; Kalita, D.; Schneider, Y.; Kessler-Kühn, J.; Schröder, S.;
963 Schubert, J.; Frankenberg, F.; Kwade, A.; Bielefeld, A.; Richter, F. H.; Janek, J. Quantifying the Impact

of Cathode Composite Mixing Quality on Active Mass Utilization and Reproducibility of Solid-State Battery Cells. *Adv. Energy Mater.* **2025.** DOI: 10.1002/aenm.202405405.

(66) Doerrer, C.; Capone, I.; Narayanan, S.; Liu, J.; Grovenor, C. R. M.; Pasta, M.; Grant, P. S. High Energy Density Single-Crystal NMC/Li6PS5Cl Cathodes for All-Solid-State Lithium-Metal Batteries. *ACS Appl. Mater. Interfaces* **2021**, *13* (31), 37809–37815. DOI: 10.1021/acsami.1c07952. Published Online: Jul. 29, 2021.

(67) Ishidzu, K.; Oka, Y.; Nakamura, T. Lattice volume change during charge/discharge reaction and cycle performance of Li[NixCoyMnz]O2. *Solid State Ion.* **2016**, *288*, 176–179. DOI: 10.1016/j.ssi.2016.01.009.

(68) Conforto, G.; Ruess, R.; Schröder, D.; Trevisanello, E.; Fantin, R.; Richter, F. H.; Janek, J. Editors' Choice—Quantification of the Impact of Chemo-Mechanical Degradation on the Performance and Cycling Stability of NCM-Based Cathodes in Solid-State Li-Ion Batteries. *J. Electrochem. Soc.* **2021**, *168* (7), 70546. DOI: 10.1149/1945-7111/ac13d2.